Draft version June 16, 2020
Typeset using LaTeX **twocolumn** style in AASTeX61

THE *R*-PROCESS ALLIANCE: J1521−3538, A VERY METAL-POOR, EXTREMELY *R*-PROCESS-ENHANCED STAR WITH [EU/FE] = +2.2, AND THE CLASS OF *r*-III STARS*

Madelyn Cain,[1] Anna Frebel,[1,2] Alexander P. Ji,[3,4] Vinicius M. Placco,[5,2] Rana Ezzeddine,[2,1] Ian U. Roederer,[6,2] Kohei Hattori,[6,7] Timothy C. Beers,[5,2] Jorge Meléndez,[8] Terese T. Hansen,[9] and Charli M. Sakari[10,2]

[1] *Department of Physics & Kavli Institute for Astrophysics and Space Research, Massachusetts Institute of Technology, Cambridge, MA 02139, USA*
[2] *Joint Institute for Nuclear Astrophysics - Center for the Evolution of the Elements, USA*
[3] *The Observatories of the Carnegie Institution of Washington, Pasadena, CA 91101, USA*
[4] *Hubble Fellow*
[5] *Department of Physics, University of Notre Dame, Notre Dame, IN 46556, USA*
[6] *Department of Astronomy, University of Michigan, Ann Arbor, MI 48109, USA*
[7] *Department of Physics, Carnegie Mellon University, Pittsburgh, PA 15213, USA*
[8] *Instituto de Astronomia, Geofísica e Ciências Atmosféricas, Universidade de São Paulo, SP 05508-900, Brazil*
[9] *The Observatories of the Carnegie Institution of Washington, 813 Santa Barbara St., Pasadena, CA 91101, USA*
[10] *Department of Physics & Astronomy, San Francisco State University, San Francisco, CA 94132, USA*

Submitted to ApJ

ABSTRACT

We report the discovery of J1521−3538, a bright (V = 12.2), very metal-poor ([Fe/H] = −2.8) strongly *r*-process enhanced field horizontal branch star, based on a high-resolution, high signal-to-noise Magellan/MIKE spectrum. J1521−3538 shows the largest *r*-process element over-abundance in any known *r*-process-enhanced star, with [Eu/Fe] = +2.2, and its chemical abundances of 22 neutron-capture elements closely match the scaled solar *r*-process pattern. J1521−3538 is also one of few known carbon-enhanced metal-poor stars with *r*-process enhancement (CEMP-*r* stars), as found after correcting the measured C abundance for the star's evolutionary status. We propose to extend the existing classification of moderately enhanced (+0.3 ≤ [Eu/Fe] ≤ +1.0) *r*-I and strongly *r*-process enhanced ([Eu/Fe] > +1.0) *r*-II stars to include an *r*-III class, for *r*-process stars such as J1521−3538, with [Eu/Fe] > +2.0 and [Ba/Eu] < −0.5, or ≥ 100 times the solar ratio of europium to iron. Using cosmochronometry, we estimate J1521−3538 to be 12.5 ± 5 Gyr and 8.9 ± 5 Gyr old, using two different sets of initial production ratios. These ages are based on measurements of the Th line at 4019 Å and other *r*-process element abundances. This is broadly consistent with the old age of a low-mass metal-poor field red horizontal branch star. J1521−3538 likely originated in a low-mass dwarf galaxy that was later accreted by the Milky Way, as evidenced by its highly eccentric orbit.

Keywords: nucleosynthesis — Galaxy: halo — stars: abundances — stars: Population II — stars: individual (2MASS J15213995−3538094)

Corresponding author: Anna Frebel
afrebel@mit.edu

* This paper includes data gathered with the 6.5 m Magellan Telescopes located at Las Campanas Observatory, Chile. Based on observations obtained at the Gemini Observatory (Prop. IDs: GS-2015A-Q-205), which is operated by the Association of Universities for Research in Astronomy (AURA), Inc., under a cooperative agreement with the National Science Foundation (NSF) on behalf of the Gemini partnership: the NSF (United States), the National Research Council (Canada), CONICYT (Chile), Ministerio de Ciencia, Tecnología e Innovación Productiva (Argentina), and Ministério da Ciência, Tecnologia e Inovação (Brazil). Based on observations collected at the European Organisation for Astronomical Research in the Southern Hemisphere under ESO programme(s) 092.D-0308(A).

1. INTRODUCTION

The atmospheres of $\sim$ 13-billion-year-old stars reflect the chemical composition of interstellar gas at the time of their birth, supplying details about element formation shortly after the Big Bang. Very metal-poor ([Fe/H] < -2.0) stars are believed to have formed from gas enriched by only one or a few progenitor supernovae or nucleosynthetic events (Frebel & Norris 2015). A very small fraction (3–5%) of these ancient stars formed from gas enriched by the rapid neutron-capture (r-) process (Barklem et al. 2005; Hansen et al. 2018; Sakari et al. 2018, R. Ezzeddine et al. 2020, in prep.). The r-process is responsible for producing the heaviest elements ($Z > 30$) in the Universe, along with the slow (s-) neutron-capture process (Karakas & Lattanzio 2014; Gull et al. 2018), and the intermediate (i-) neutron-capture process (Dardelet et al. 2014; Hampel et al. 2016). The observed elemental abundance patterns of metal-poor r-process-enhanced stars can thus be used to characterize the yields of r-process production events and associated sites in the early Universe.

The r-process principally occurs when seed nuclei (e.g., iron-group elements) are bombarded rapidly with neutrons, resulting in neutron-rich, unstable isotopes. A distinct chemical abundance pattern of heavy elements up to and including uranium is created from the radioactive decay of these isotopes. Evidence from stars displaying the r-process pattern, including the Sun and metal-poor stars (e.g., Sneden et al. 1996; Hill et al. 2002; Frebel et al. 2007; Casey & Schlaufman 2017; Placco et al. 2017; Holmbeck et al. 2018; Sakari et al. 2018), strongly suggests that the pattern is universal across cosmic time, at least for elements Ba to Hf. This behavior has been associated with the main component of the r-process (the "main-r-process") (Truran et al. 2002). On the contrary, variations can exist between lighter elements ($38 \leq Z < 56$) and the corresponding scaled-solar r-process pattern (e.g., Barklem et al. 2005; Roederer et al. 2014a; Ji et al. 2016b; Ji & Frebel 2018; Cain et al. 2018). These variations might be caused by a "limited r-process" which is postulated to only produce neutron-capture elements lighter than barium (Wanajo et al. 2001; Travaglio et al. 2004). Additionally, the abundances of the actinide elements Th and U occasionally deviate from the scaled-solar r-process pattern in the form of stars displaying an "actinide-boost" (e.g., Mashonkina et al. 2014; Holmbeck et al. 2018) or an actinide deficiency (e.g., Ji & Frebel 2018).

Decades of observational and theoretical efforts have been devoted towards understanding the origins of the r-process (see Frebel 2018 and references therein). Evidence from the "kilonova" electromagnetic counterpart of the merger of a neutron star pair GW170817 (Abbott et al. 2017a,b) strongly supports neutron star mergers as viable main r-process sites (Coulter et al. 2017; Drout et al. 2017; Kilpatrick et al. 2017; Shappee et al. 2017). Simulations also show that collapsar (the collapse of rapidly rotating massive stars) accretion disks may yield sufficient r-process elements to explain a significant contribution to the Universe's main r-process enrichment (Surman et al. 2006; Siegel et al. 2019). The limited r-process may occur during core-collapse supernovae, through a high-entropy neutrino wind (e.g., Meyer et al. 1992; Woosley & Hoffman 1992; Kratz et al. 2007; Arcones & Montes 2011; Wanajo 2013) or jet-like explosions during magnetorotationally driven core-collapse supernovae (Nishimura et al. 2015).

The amount of r-process enhancement in metal-poor stars can provide constraints on the yields and astrophysical sites of the r-process(es) if the mass of the birth gas clouds is known. Observational evidence from the r-process-rich ultra-faint dwarf (UFD) galaxy Reticulum II first suggested that the astrophysical site of the main r-process was a prolific event such as a neutron star merger (Ji et al. 2016a,b; Roederer et al. 2016). The gas dilution mass of Reticulum II and the level of r-process-enhancement from several of its metal-poor stars were used to estimate the yield of the rare r-process event that enriched the galaxy, consistent with that of a single neutron star merger.

While r-process stars in UFDs can provide constraints on the yields of r-process events, UFD stars are particularly difficult to observe due to their faint magnitudes. On the contrary, metal-poor r-process-enhanced Galactic halo stars are generally brighter and can be easily observed to obtain a very-high-S/N spectrum for detailed chemical abundance analysis. R-process enhancement is also not restricted to any particular evolutionary status, making it possible to use different samples to discover them. Nevertheless, most searches have focused on cooler giants whose absorption lines are stronger and thus easier to measure when elemental abundances are low.

About half of metal-poor r-process-enhanced halo stars have been estimated to be accreted from now-destroyed r-process UFDs such as Reticulum II (Brauer et al. 2019). The natal gas cloud masses from which halo stars originally formed, however, remain unknown, so that r-process yields cannot be inferred. Information about their birth sites may instead be inferred from their kinematics (Roederer et al. 2018a) and chemical abundances. Statistically large samples of ancient r-process

halo stars can thus help trace the origins of r-process enhancement in the Galaxy shortly after the Big Bang.

The goal of the R-Process Alliance (RPA; Hansen et al. 2018) is to better understand the r-process and its astrophysical production site(s) by increasing the number of known r-process-enhanced stars in the Milky Way. Recent results from the RPA include detailed chemical abundances of both strongly enhanced r-II stars ([Eu/Fe] $> +1.0$) and moderately enhanced r-I stars ($+0.3 \leq$ [Eu/Fe] $\leq +1.0$) in the Galactic halo (e.g., Cain et al. 2018; Hansen et al. 2018; Holmbeck et al. 2018; Roederer et al. 2018b; Sakari et al. 2018, 2019). We here present a newly discovered very metal-poor ([Fe/H]= −2.80) red horizontal branch star, 2MASS J15213995−3538094 (hereafter J1521−3538), found as part of the ongoing discovery work of the RPA. J1521−3538 is extremely r-process-enhanced with [Eu/Fe]= +2.2, the highest value of any r-process-enhanced star known to date. J1521−3538 is also one of a small but growing number of r-process-enhanced horizontal branch stars. In this paper we describe the chemical abundance pattern of J1521−3538, and introduce a new regime in the parameter space of extreme r-process-enhancement in very metal-poor stars.

2. OBSERVATIONS AND LINE MEASUREMENTS

J1521−3538, with α = 15:21:39.8, δ = −35:38:08.3, V = 12.2, was first identified as a potential metal-poor star from photometry (based on the criteria of Meléndez et al. 2016) and spectroscopy in RAVE DR5 (Kunder et al. 2017). The star was followed-up with medium-resolution ($R \sim 2,000$) spectroscopy using the ESO New Technology Telescope (EFOSC-2; semester 2014A) and the Gemini South Telescope (GMOS-S; semester 2015A). Both observing setups used similar gratings (~ 600 l mm^{-1}) and slits ($\sim 1\farcs0$) in blue setup, to cover at least the wavelength range $\sim$ 3800-5300 Å and exposure times to yield signal-to-noise (S/N) ratios of S/N $\sim$ 50 per pixel at $\sim$ 3930 Å. Further details on the observations, data reduction, and processing can be found in Placco et al. (2018). Atmospheric parameters and carbon abundances were determined from the final, combined spectra using the n-SSPP (Beers et al. 2014, 2017): $T_{\rm eff}$ = 6029 K, $\log g$ = 3.02, [Fe/H] = −2.96, [C/Fe] = +1.34. Additional medium resolution stellar parameters are listed in Table 1.

We then observed J1521−3538 using the Magellan-Clay telescope and the MIKE spectrograph (Bernstein et al. 2003) at Las Campanas Observatory on 2016 April 16 and 2017 May 6. We obtained a high-resolution spectrum with nominal resolving power of $R \sim 35,000$ in the blue and $R \sim 28,000$ in the red wavelength regime, using a $0\farcs7$ slit and 2×2 binning. The spectra cover $\sim$ 3500 Å to $\sim$ 9000 Å, with the blue and red CCDs overlapping at around $\sim$ 5000 Å. The total exposure time was 15 minutes in 2016 and 20 minutes in 2017. Data reductions were completed using the MIKE Carnegie Python pipeline (Kelson 2003). To combine the data from both nights, we first reduced the data from each night separately. The reduced spectra from both nights were combined after shifting each to the rest frame to account for spatial and spectral shifts between nights. The resulting S/N for the combined spectrum is 110 at 4000 Å, 150 at 4500 Å, and 200 at 6000 Å. Representative portions of the spectrum, including the Eu II line at 4130 Å, the Ba II line at 5853 Å, and the Th II line at 4019 Å, are shown in Figure 1.

We measured heliocentric radial velocities ($v_{\rm helio}$) by cross-correlating the two individual spectra against a template spectrum of HD 140283. Although HD 140283 is a subgiant star, it is an ideal candidate for radial velocity cross-correlation because it has a similar effective temperature and metallicity to J1521−3538 (see Section 3). We find $v_{\rm helio}$ values of $+79.32 \pm 0.9$ km s^{-1} and $+81.43 \pm 1.3$ km s^{-1} for the 2016 and 2017 observations, respectively. We derive uncertainties from the standard deviation of $v_{\rm helio}$ measurements found using several different template spectra. The resulting uncertainties agree with the level of stability of MIKE. We adopt a final heliocentric radial velocity of 80.38 km s^{-1} by averaging our results and an uncertainty of ± 0.84 km s^{-1} by inverse variance weighting.

Table 1. Stellar Parameters

Source	$T_{\rm eff}$ [K]	log g [cgs]	$v_{\rm micr}$ [km s^{-1}]	[Fe/H]
High-Resolution Stellar Parameters				
LTE	5850	2.10	2.65	−2.80
NLTE	5780	2.75	2.10	−2.54
Medium-Resolution Stellar Parameters				
RAVE DR5	5586	2.84	...	−2.00
RAVE-on[a]	6091	3.70	...	−1.47
n-SSPP	6029	3.02	...	−2.96

NOTE—High-resolution LTE parameters are adopted for our chemical abundance analysis.
[a]Casey et al. (2017)

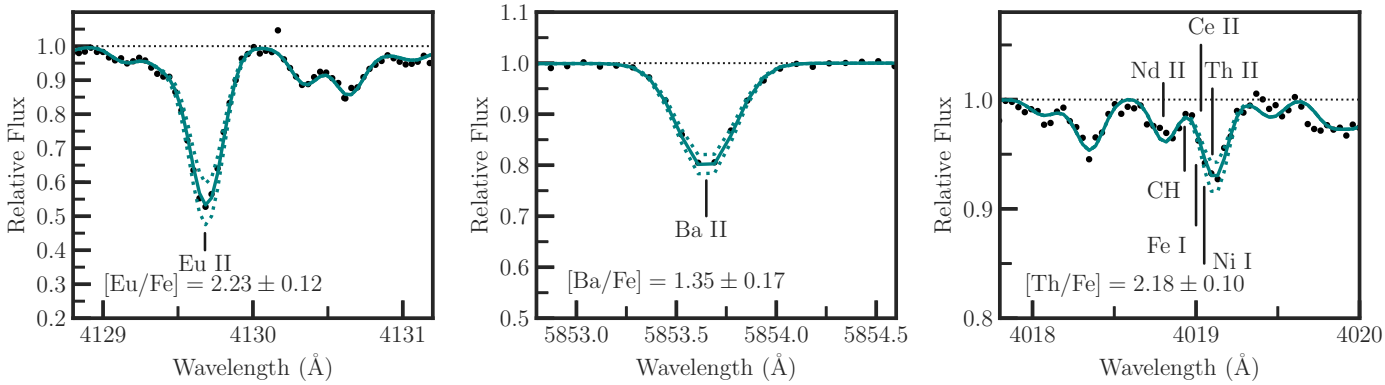

Figure 1. Portions of the Magellan/MIKE spectrum of J1521−3538 (black dotted lines) near the Eu II line at 4130 Å (left), the Ba II line at 5853 Å (middle), and the Th II line at 4019 Å (right). Best-fit synthetic spectra are shown in solid teal with abundance variations of ±0.14, ±0.10, and ±0.10 dex in dashed teal for the Eu II, Ba II, and Th II lines, respectively.

Previous survey observations also report v_{helio} values for J1521−3538. RAVE DR5 (Kunder et al. 2017) reports a heliocentric radial velocity of $+79.26 \pm 1.84\,km\,s^{-1}$ from 2005 May 28. Gaia DR2 records a radial velocity of $+79.44 \pm 0.89\,km\,s^{-1}$ collected between 2014 July 25 and 2016 May 23 (Gaia Collaboration et al. 2016a,b). These measurements, along with our data, suggest that J1521−3538 is a single star, in line with the majority of metal-poor *r*-process-enhanced stars (Hansen et al. 2015b).

We then performed a standard abundance analysis for our star following the procedure described in Frebel et al. (2013). We used the 2017 version of the `MOOG` code[1] (Sneden 1973), which accounts for Rayleigh scattering as coherent, isotropic scattering (Sobeck et al. 2011). Together with MOOG, we employ an `ATLAS9` (Castelli & Kurucz 2004) 1D plane-parallel model atmosphere with α-enhancement and no overshooting, and assuming local thermodynamic equilibrium (LTE). All line measurements, stellar parameters, and abundance measurements were made using the `SMHR` software (Casey 2014).

We derived iron equivalent widths (EW) using a line list compiled from several data sources (O'Brian et al. 1991; Kurucz 1998; Meléndez & Barbuy 2009; Den Hartog et al. 2014; Ruffoni et al. 2014). Neutron-capture line lists used data from Hill et al. (2002, 2017). Synthesis line lists based on atomic data from Sneden et al. (2009, 2014, 2016) were provided by Chris Sneden and supplemented with data from Kurucz (1998). The CH synthesis line list was taken from Masseron et al. (2014).

We obtained EW measurements by fitting a χ^2-minimized Gaussian profile to each absorption line in our list. Lines with strong damping wings were disregarded. In addition, we performed synthesis measurements for heavily blended lines or lines with hyperfine structure by fitting the line of interest and any surrounding lines within a local wavelength region by using already measured abundances. We obtained a 3σ upper limit on the abundance of lines too weak to be detected. [X/H] and [X/Fe] values were calculated using solar abundances from Asplund et al. (2009). Wavelengths (λ), excitation potentials (EP), $\log gf$ values, EWs, and derived abundances ($\log \epsilon$) are listed in Table 2.

Table 2. Line list and derived abundances for J1521−3538

Element	λ [Å]	EP [eV]	log *gf*	EW [mÅ]	log ϵ(X)
CH	4312	...	...	syn	6.20
Na I	5889.95	0.00	0.11	121.0	3.69
Na I	5895.92	0.00	−0.19	89.7	3.54
Mg I	3986.75	4.35	−1.03	12.9	5.25
Mg I	4057.51	4.35	−0.89	11.0	5.03
Mg I	4167.27	4.35	−0.71	23.2	5.22
Mg I	4702.99	4.33	−0.38	35.9	5.10
Mg I	5528.40	4.34	−0.50	32.7	5.16
Mg I	5711.09	4.34	−1.72	3.4	5.30
Al I	3944.00	0.00	−0.64	syn	2.93
Al I	3961.52	0.01	−0.34	79.4	2.88
Si I	3906.52	1.91	−1.09	syn	4.79
Ca I	4283.01	1.89	−0.22	20.2	3.86
Ca I	4318.65	1.89	−0.21	21.8	3.89

NOTE—"syn" denotes spectrum synthesis was used to measure the abundance. For ease of reading, we include the full list at the end of the paper in Table 7.

[1] https://github.com/alexji/moog17scat

3. STELLAR PARAMETERS

Stellar parameters for J1521−3538 were determined spectroscopically using EWs from 154 Fe I and 21 Fe II lines following the procedure in Frebel et al. (2013). Our final adopted stellar parameters are $T_{\rm eff}$ = 5850 K, $\log g$ = 2.10, [Fe/H] = −2.80, and $v_{\rm micr}$= 2.65 km s^{-1}. These parameters are consistent with the star being located on the red horizontal branch, as gleaned from a 12.7 Gyr isochrone from the PARSEC models (Marigo et al. 2017)[2] for [Fe/H] = −2.2. We note here that technically, horizontal branch stars were not included in the Frebel et al. (2013) stellar parameter calibration. However, a sample of five horizontal branch stars (A. Frebel et al. 2020, in prep.) suggests that in order to adequately deal with abundances of strong lines, significant effective temperate decreases (together with higher $v_{\rm micr}$ values) are necessary to bring these abundances in line with those of weaker lines. The resulting cooler temperatures are not unlike those investigated in Frebel et al. (2013). While this issue is being explored, we preemptively decided to apply the non-horizontal branch correction to J1512-3538, as a mitigation. We adopt typical systematic uncertainties in the stellar parameters as obtained from a spectroscopic analysis (Frebel et al. 2013; Ji et al. 2016a). We take $\sigma_{\rm T_{eff}}$ = 150 K, $\sigma_{\log g}$ = 0.30 dex, and $\sigma_{v_{\rm micr}}$ = 0.30 km s^{-1}. Statistical contributions to $\sigma_{\rm T_{eff}}$, $\sigma_{\log g}$, and $\sigma_{v_{\rm micr}}$ are negligible in comparison, due to the brightness of J1521−3538 (V = 12.2), the high S/N of the spectrum, and the large number of Fe I lines measured. The uncertainty in [Fe/H] is 0.15 dex, which is derived from the standard deviation of Fe I line abundances. Our stellar parameters agree well with results from the EFOSC/GMOS medium-resolution spectrum and results from RAVE surveys (see Table 1).

We also determined stellar parameters assuming non-LTE (NLTE). Deviations from LTE are significant for minority species, such as Fe I. These NLTE effects are particularly strong in metal-poor stars, as they have lower atmospheric electron densities and fewer atomic collisions. Thus, stellar parameters derived assuming NLTE are generally more accurate than the LTE parameters. To determine NLTE stellar parameters, we first determined NLTE abundances for Fe I and Fe II lines using a comprehensive Fe atom (Ezzeddine et al. 2016) with up-to-date atomic data, especially for hydrogen collisions from Barklem (2018). Starting from the LTE stellar parameters, we changed each parameter iteratively until excitation and ionization equilibrium were attained in NLTE between abundances of Fe I and Fe II lines. Using this procedure, outlined in Ezzeddine et al. (2017), we derived NLTE stellar parameters of $T_{\rm eff}$ = 5780 ± 112 K, $\log g$ = 2.75 ± 0.45 dex, [Fe/H] = −2.54±0.15, and $v_{\rm micr}$ = 2.10 ± 0.45 km s^{-1}. The uncertainties listed are those determined in Ezzeddine et al. (2018) for metal-poor stars with detectable Fe II lines, which we adopt here. The derived temperature and surface gravity are consistent with J1521−3538 being a red horizontal branch star. The derived NLTE metallicity of −2.54 agrees well with the predicted NLTE metallicity of −2.56 from the Ezzeddine et al. (2017) equation

$$[\mathrm{Fe/H}]_{\rm NLTE,\ predicted} = 0.86 \times [\mathrm{Fe/H}]_{\rm LTE} - 0.15.$$

Since the metallicity was increased and Fe I is primarily affected by NLTE, the surface gravity had to also be increased by 0.65 dex to reach ionization balance. The NLTE microturbulence was lowered by 0.55 km s^{-1}. However, in order to readily calculate consistent abundance ratios and to compare our results to literature values, we use the LTE parameters for the chemical abundance analysis and interpretation throughout the paper. Future capabilities able to produce full NLTE abundance patterns would hopefully make use of our NLTE stellar parameters.

4. CHEMICAL ABUNDANCES

We obtained abundance measurements using both spectrum synthesis and EW analysis. Our final abundances are summarized in Table 3 and fully detailed in Table 2. We derive statistical abundance uncertainties, σ, from the standard deviation of line abundances, which was corrected for small samples when five or fewer lines were measured. Systematic uncertainties due to, e.g., NLTE effects, 1D stellar model atmospheres, and gf-values, are not explicitly considered. Small sample standard deviations for elements with measured abundances of 2–5 lines were obtained following Keeping (1962), by multiplying the range of values covered by our line abundances with the k-factor calculated for small samples. For elements with one line only, we adopt an uncertainty between 0.1 and 0.3 dex, depending on the data and fit quality. Finally, we adopt a minimum uncertainty of 0.10 dex, as better precision is improbable due to continuum placement difficulties. Table 4 enumerates the systematic uncertainties in our chemical abundances resulting from uncertainties in our model atmosphere parameters, obtained from varying the stellar parameters by their uncertainties in the positive direction ($\sigma_{\rm T_{eff}}$ = +150 K, $\sigma_{\log g}$ = +0.30 dex, $\sigma_{v_{\rm micr}}$ = +0.30 km s^{-1}), and recording the resulting change in abundance.

[2] http://stev.oapd.inaf.it/cgi-bin/cmd

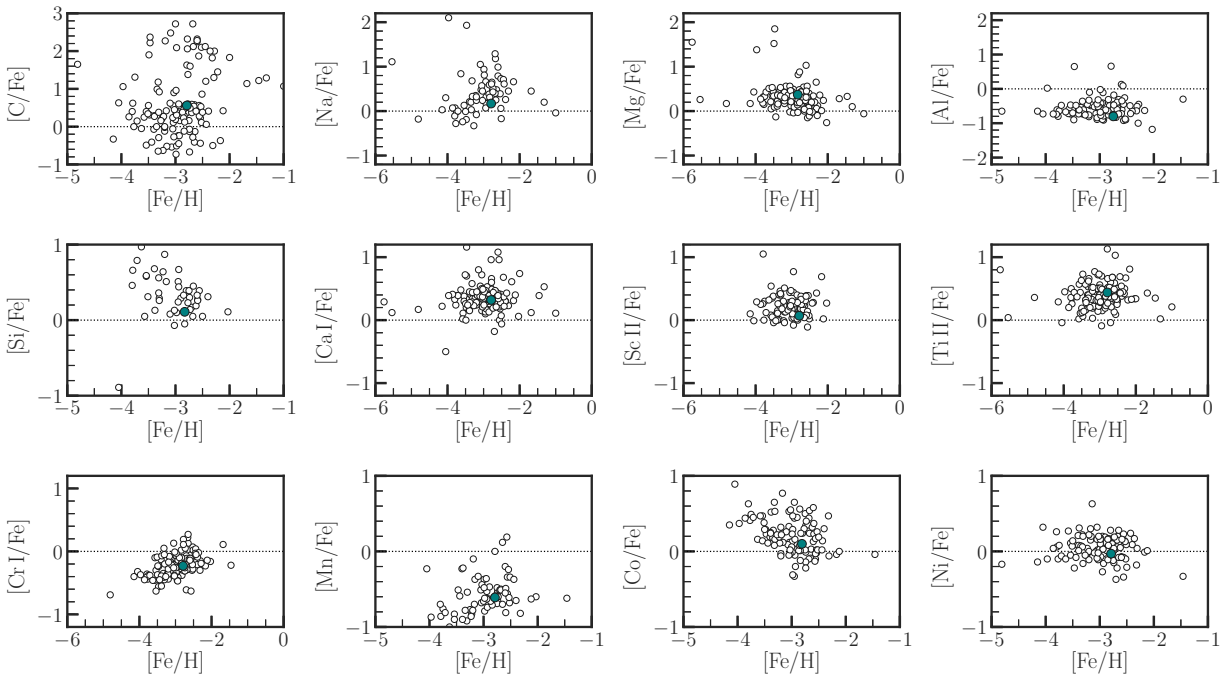

Figure 2. Light-element abundances for J1521−3538 (teal filled circles) together with abundances for other metal-poor stars from Yong et al. (2013). Abundances for C and Na are not corrected for evolutionary status or NLTE behavior in this figure.

4.1. *Light Elements*

We measured light-element abundances (C, Na, Mg, Al, Si, Ca, Sc, Ti, V, Cr, Mn, Co, Ni, and Zn) for J1521−3538. They are in agreement with the abundances of other metal-poor stars analyzed by Yong et al. (2013), as can be seen in Figure 2. We note that we did not measure O (e.g., from the O I 6300 Å line) or K (e.g., from the K I 7664 Å line), as they were too weak to be measured, and blended with telluric features.

Carbon. We measured a carbon abundance of [C/Fe] = +0.56 by performing spectrum synthesis on the CH G-bandhead at 4313 Å and assuming [O/Fe] = +0.00. The CH feature at 4323 Å was too weak to be measured. We estimate a low value consistent with 4 (the approximate equilibrium value of the CN cycle) for the $^{12}C/^{13}C$ ratio from the line at 4217 Å, supporting our assertion that J1521−3538 is a horizontal branch star. For the same reason, its carbon abundance can be assumed to be depleted by the CN cycle having operated during the star's evolution along the giant branch. Therefore, we correct the carbon abundance to account for its evolutionary status to obtain an abundance more representative of the natal gas cloud from which J1521−3538 formed. We apply the maximum correction of +0.59 dex following Placco et al. (2014), yielding a corrected carbon abundance of [C/Fe] = +1.15. J1521−3538 adds to the small number of known *r*-process rich carbon-enhanced metal-poor stars (CEMP-*r*; with [C/Fe] > +0.70; Beers & Christlieb 2005; Aoki et al. 2007).

Sodium and Aluminum. Sodium abundances ([Na/Fe] = +0.17) are derived from the EWs of the Na doublet at 5890 Å and 5895 Å. There are about seven interstellar medium (ISM) Na features which are clearly spread apart and separate from the stellar lines. It can never be excluded that there is an ISM feature at the same velocity as the star, but since the two Na lines give consistent abundances, it is likely that the stellar lines are not affected. We apply non-LTE corrections to the Na abundance using results from Lind et al. (2011), yielding a corrected value of [Na/Fe] = −0.06. We measure the aluminum abundance ([Al/Fe] = −0.76) from spectrum synthesis of the Al I line at 3944 Å and an EW measurement of the Al I at 3961 Å. The abundances derived from both lines exhibit excellent agreement, with $\log \epsilon$(Al) values of 2.93 and 2.88, respectively.

Magnesium, Silicon, Calcium, Titanium. The abundances of Mg, Si, Ca, and Ti (also known as α-elements) were obtained using a mixture of EW measurements and spectrum synthesis. We measured the Si line at 3905 Å using spectrum synthesis. The Si I line at 4102 Å was heavily blended and could not be measured. The abundances of the α-elements were [Mg/Fe] = +0.42, [Si/Fe] = +0.11, [Ca/Fe] = +0.32, and [Ti/Fe] = +0.31. This level of α-element enhancement ([α/Fe] $\sim$ +0.4) is consistent with stars whose

Table 3. Chemical Abundances of J1521−3538

Element	log ϵ(X)	[X/H]	[X/Fe]	N	σ
C	6.20	−2.23	0.56	1	0.30
Na I	3.62	−2.62	0.17	2	0.10
Mg I	5.14	−2.46	0.37	10	0.08
Al I	2.90	−3.55	−0.76	2	0.10
Si I	4.79	−2.72	0.11	1	0.20
Ca I	3.87	−2.47	0.32	1	0.13
Sc II	0.43	−2.72	0.07	8	0.10
Ti I	2.60	−2.35	0.44	8	0.16
Ti II	2.46	−2.49	0.31	37	0.13
V II	1.32	−2.12	0.18	2	0.10
Cr I	2.62	−3.02	−0.23	7	0.10
Mn I	1.89	−3.54	−0.75	4	0.10
Fe I	4.71	−2.79	0.00	154	0.15
Fe II	4.72	−2.78	0.01	21	0.10
Co I	2.28	−2.71	0.08	3	0.10
Ni I	3.40	−2.82	−0.03	14	0.16
Zn I	1.80	−2.76	0.03	1	0.20
Sr II	1.24	−1.63	1.16	1	0.20
Y II	0.45	−1.76	1.03	11	0.11
Zr II	1.13	−1.54	1.35	8	0.13
Ru I	0.89	−0.86	1.93	1	0.20
Ba II	0.74	−1.44	1.35	2	0.17
La II	0.12	−0.98	1.81	18	0.10
Ce II	0.43	−1.15	1.64	20	0.10
Pr II	−0.15	−0.87	1.92	8	0.10
Nd II	0.45	−0.97	1.82	46	0.10
Sm II	0.10	−0.86	1.93	13	0.10
Eu II	−0.04	−0.56	2.23	7	0.12
Gd II	0.45	−0.62	2.17	9	0.13
Tb II	−0.37	−0.67	2.13	3	0.16
Dy II	0.45	−0.65	2.14	5	0.10
Ho II	−0.30	−0.78	2.01	9	0.10
Er II	0.21	−0.71	2.08	5	0.11
Tm II	−0.62	−0.72	2.07	5	0.15
Yb II	0.02	−0.82	1.97	1	0.20
Hf II	−0.03	−0.88	1.91	1	0.20
Os I	0.90	−0.50	2.33	1	0.30
Ir I	< 1.53	< 0.15	< 2.94	1	...
Th II	−0.60	−0.61	2.18	1	0.10
U II	< −0.59	< −0.05	< 2.75	1	...

Table 4. Systematic Uncertainties

Element	$\Delta T_{\rm eff}$ +150 K	Δ log(g) +0.30 dex	$\Delta v_{\rm micr}$ +0.30 km s^{-1}	Total Error
C	+0.10	−0.28	−0.25	0.38
Na I	+0.10	−0.02	−0.07	0.12
Mg I	+0.07	−0.05	−0.10	0.13
Al I	+0.15	−0.03	−0.01	0.15
Ca I	+0.09	−0.01	−0.01	0.11
Ti I	+0.14	+0.00	+0.00	0.14
Ti II	+0.08	+0.10	−0.03	0.13
Cr I	+0.16	−0.01	−0.03	0.16
Fe I	+0.13	−0.01	−0.04	0.14
Fe II	+0.03	+0.10	−0.02	0.11
Ni I	+0.21	−0.04	−0.08	0.23
Zn I	+0.10	+0.01	−0.01	0.08
Sr II	+0.06	+0.13	+0.04	0.15
Ba II	+0.08	+0.10	−0.04	0.13
Ce II	+0.05	+0.05	−0.05	0.09
Nd II	+0.11	+0.11	−0.01	0.16
Eu II	+0.06	+0.07	+0.02	0.09
Er II	+0.14	+0.08	−0.02	0.16
Os I	+0.15	+0.14	−0.19	0.28
Th II	+0.07	+0.07	+0.00	0.10

NOTE—The individual systematic errors are added in quadrature to compute the total error.

light-element abundance enhancement originates primarily from core-collapse supernovae, rather than Type Ia supernovae. The low Si abundance is likely a model atmosphere effect because J1521−3538 is a hot horizontal branch star (cf. Preston et al. 2006), so the measured abundance likely does not reflect the true cosmic abundance.

Scandium through Zinc. Sc was measured from eight equivalent widths, yielding an abundance of [Sc/Fe] = 0.09. V was measured using spectrum synthesis of the 3952 Å line and the 4005 Å line. The abundances derived from these lines agreed well, with [V/Fe] values of +0.17 and +0.18, respectively. Ni and Cr were measured from several lines using EW measurements, whereas Mn and Co were measured using synthesis measurements. Zinc ([Zn/Fe] = +0.03) was measured from the EW of the strongest available line at 4810 Å. No other Zn lines were detectable. We adopt a conservative error estimate for Zn of 0.20 dex, because this line was in fact very weak.

4.2. *Neutron-Capture Elements*

We derive abundances for 22 neutron-capture elements for J1521−3538. Measurements or 3σ upper limits for Sr, Y, Zr, Ru, Ba, La, Pr, Sm, Eu, Tb, Dy, Ho, Tm, Yb, Hf, Os, Ir, Th, and U were measured with spectrum synthesis to account for hyperfine structure and blending of absorption features. Abundances based on EWs were obtained for Ce, Nd, Gd, and Er. For Ba and Eu measurements, we used the *r*-process isotope composition as given in Sneden et al. (2008). Mo, Pd, Ag, Lu, and Pb could not be measured. Abundance results and uncertainties are given in Table 3. The full set of line abundances and associated atomic data of all measured elements are presented in Table 2. Figure 3 displays our

neutron-capture element abundances overlaid with the scaled solar r-process pattern from Burris et al. (2000). We scaled the solar r-process pattern by the difference between the mean measured abundances for elements Ba to Yb in J1521−3538 and the Sun.

Strontium, Yttrium, Zirconium. Using spectrum synthesis, we measured the Sr abundance from the line at 4161 Å, as the lines at 4077 Å and 4215 Å were saturated. Y and Zr were measured from 10 and 8 lines, respectively. These elements are just slightly heavier than those at the first r-process peak and may be produced by the limited r-process (Wanajo & Ishimaru 2006; Siqueira Mello et al. 2014). Because the limited r-process is thought to occur at different astrophysical site(s) than the main r-process, the abundances of Sr, Y, and Zr are often offset from the main r-process pattern. In the case of J1521−3538, however, the Sr and Zr abundances agree very well with the scaled solar r-process pattern, as shown in Figure 3. The Y residual is larger (~ 0.5 dex), though this deviation is common and can be attributed to our choice of solar r-process pattern, so it should not be regarded as a concern (Arlandini et al. 1999). The overall agreement between Sr, Y, and Zr and the main r-process elements with the scaled solar r-process pattern indicates that J1521−3538 likely inherited a substantial amount of material from the main r-process.

Barium through Hafnium. Two barium lines were measured using spectrum synthesis at 4130 Å and 5853 Å. The 4130 Å line was blended with Gd and Ce, but a good fit was obtained using the independently measured Gd and Ce abundances. The line at 5853 Å is clean, and is shown in Figure 1. Its abundance agreed well with the 4130 Å line, yielding an overall uncertainty of 0.11 dex. The Ba lines at 4553 Å, 6142 Å, and 6497 Å were saturated. A total of 18 lanthanum lines were measured between 3795 Å and 5123 Å using spectrum synthesis. All line abundances agreed within 0.3 dex. Cerium, neodymium, and gadolinium abundances were derived from the EWs of 20, 46, and 9 lines, respectively. The uncertainties on these measurements were low (~ 0.10 dex) due to the large number of lines measured and low spread (~ 0.30 dex).

Eight praseodymium lines were measured between 4063 Å and 4449 Å. Spectrum synthesis was used to account for the hyperfine structure. The lines at 4179 Å and 4449 Å were blended with Nd II and Dy II, respectively. Nevertheless, the derived abundances were consistent with other values, with an overall uncertainty of 0.10 dex. Samarium was also measured from 13 lines using spectrum synthesis. All of the measured Sm lines were weak; however, the derived abundance of $\log\epsilon(\mathrm{Sm}) = 0.10 \pm 0.10$ agrees well with the scaled solar r-process pattern in Figure 3.

We measured the europium abundance from seven lines at 3725 Å, 3820 Å, 3907 Å, 4129 Å, 4205 Å, 6645 Å, and 7218 Å. The 4129 Å line is shown in Figure 1. We used an isotope ratio of $^{151}\mathrm{Eu}/^{153}\mathrm{Eu} = 0.88$, following Sneden et al. (2008). Lines at 6645 Å and 7218 Å were weaker, whereas the other five lines were strong. The 3725 Å line was located in the wing of a Balmer line, so the continuum was fit locally. The final abundance for the line at 3725 Å (with $\log\epsilon(\mathrm{Eu}) = -0.11$) agreed well with the average line abundance ($\log\epsilon(\mathrm{Eu}) = -0.04$). The line at 7218 Å yielded the highest abundance (+0.22) and was included due to its high quality (no blending or distortions). The 4205 Å line had the lowest abundance (−0.16), but the overall fit was very good. We find $[\mathrm{Eu/Fe}] = +2.23 \pm 0.12$, with a standard deviation in $\log\epsilon(\mathrm{Eu})$ values of 0.12 dex.

We measured Tb, Dy, Ho, Yb, and Hf using spectrum synthesis, and Er using EW measurements. We measured Tb from three lines at 3569 Å, 3659 Å, and 3899 Å. The line at 3702 Å was located in the wing of a Balmer line and could not be measured. Although the 3569 Å and 3659 Å lines were located in noisier portions of the spectrum, all line measurements agreed well with the average value of $[\mathrm{Tb/Fe}] = +2.13$, within 0.20 dex. The $\log\epsilon(\mathrm{Dy})$ measurements were remarkably consistent, with a range of values of 0.05 dex. We measured the 4077 Å Dy line with spectrum synthesis. This required increasing the abundance of the strong blending Sr line by an artificial ~ 0.40 dex to account for the saturation of the contributing line. We measured Yb from one line at 3694 Å, and adopt a conservative uncertainty of 0.20 dex. Hf was measured from one line at 4093 Å, yielding an abundance of $\log\epsilon(\mathrm{Hf}) = -0.03$. The Hf line at 3917 Å was excluded because it was heavily blended, though we note its abundance (0.06) agrees well with our adopted abundance.

Overall, the chemical abundances of barium through hafnium show remarkable agreement with the scaled solar r-process pattern shown in Figure 3.

Osmium and Iridium. We determined the Os abundance from the line at 4419 Å using spectrum synthesis. We adopt an uncertainty of 0.30 dex to account for the quality of the line, which was very weak and heavily blended with Sm. This measurement yielded an abundance of $[\mathrm{Os/Fe}] = 2.33$ ($\log\epsilon(\mathrm{Os}) = 0.90$). Our adopted abundance agrees within 1σ with the scaled solar r-process pattern. We also obtained consistent 3σ upper limits of $\log\epsilon(\mathrm{Os}) = 1.20$ and $\log\epsilon(\mathrm{Os}) = 1.61$ from two weak lines at 4260 Å and 4136 Å, respectively.

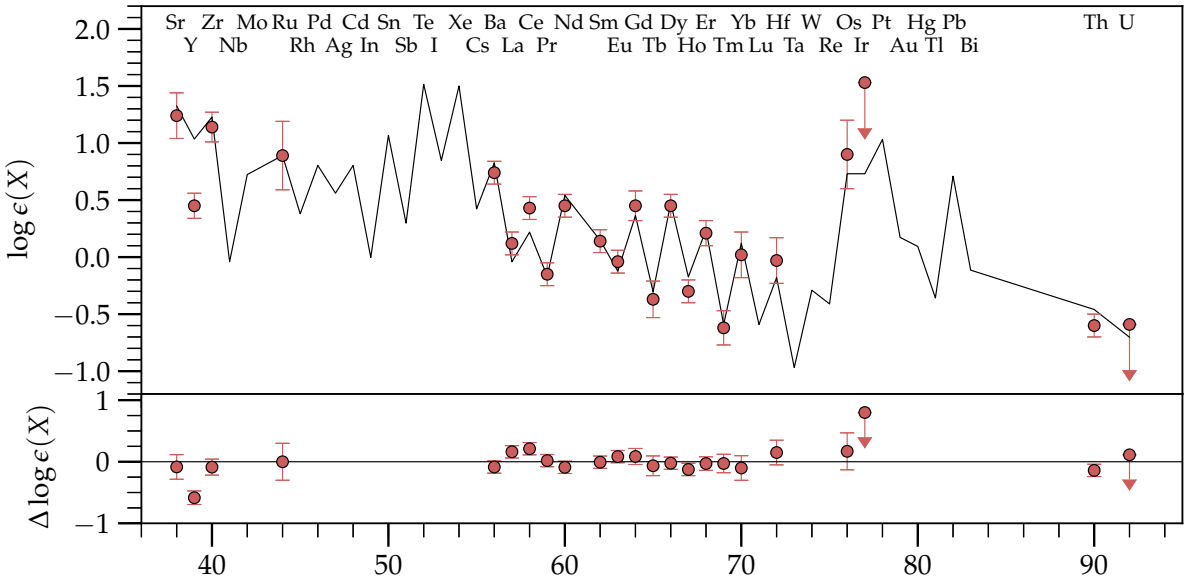

Figure 3. *R*-process elemental abundance pattern for J1521−3538 overlaid with a scaled solar *r*-process pattern (Burris et al. 2000) (top). Residuals between the measured abundances and the scaled solar *r*-process pattern are also shown (bottom).

A 3σ upper limit for Ir was measured from the line at 3513 Å, yielding an abundance of $\log\epsilon(\mathrm{Ir}) < 1.53$. A tighter bound on the abundance upper limit of $\log\epsilon(\mathrm{Ir}) < 1.13$ was derived from the line at 3800 Å, but this was value was not adopted because the line was blended with a Balmer line. Instead, we adopt the more conservative upper limit from the 3513 Å line.

Thorium and Uranium. We determined the Th abundance from the line at 4019 Å, taking into account various blends (e.g., C, Fe, Ni, Ce, Pr). The fit, which yielded [Th/Fe] = +2.18, is shown in Figure 1. Abundance variations of ±0.10 dex are also given to show the quality of the fit. For U, only an upper limit could be determined from a synthetic fit of the line at 3859 Å. This line is located on the wing of a saturated Fe line, so we increased the Fe abundance by 0.49 dex to obtain a better fit. We adopt a final conservative, 3σ upper limit of [U/Fe] < +2.75.

Thorium and uranium are radioactive isotopes solely produced by the *r*-process. J1521−3538 does not appear to have an unusual amount of Th ("actinide boost") compared to expectations of the decay and taking into account its presumably old age. This makes it possible to estimate a stellar age for J1521−3538, by comparing abundance ratios involving Th with theoretical *r*-process production ratios, as further described in Section 5.3.

5. DISCUSSION AND CONCLUSION

5.1. *The Class of r-III Stars*

J1521−3538 is the second *r*-process enhanced star with a [Eu/Fe] abundance larger than +2.0; i.e., the abundance ratio is enhanced by a factor of > 100 compared to the solar ratio. This is shown in Figure 4. At [Fe/H] = −2.8, this implies that J1521−3538 contains only 4 times less Eu than the Sun. The other such star known is J0334−5405, with [Eu/Fe] = +2.11, a star in the *r*-process dwarf galaxy Reticulum II (Ji et al. 2016a; Roederer et al. 2016). Though its absolute Eu abundance is very similar to that of J1521−3538, the result was not initially considered significant because the S/N of the spectrum was fairly low. Given this leap by more than a factor of two in *r*-process enhancement compared to previously known *r*-process rich stars (with [Eu/Fe] $\lesssim$ +1.9), we propose to extend the existing classification scheme (Beers & Christlieb 2005) to include an "*r*-III" class for stars with [Eu/Fe] > +2.0. The other classes are the moderately enhanced (+0.3 ≤ [Eu/Fe] ≤ +1.0) *r*-I and the strongly enhanced *r*-process ([Eu/Fe] > +1.0) *r*-II stars. The three classes are illustrated in Figure 4. The *r*-I stars make up about 15% of metal-poor halo stars with [Fe/H] $\lesssim$ −2.0, whereas *r*-II stars are less common with ∼ 3-5% (Barklem et al. 2005; Sakari et al. 2018). The *r*-III stars are thus extremely rare, making up roughly 5% of all *r*-II stars (excluding J0334−5405), which implies a frequency of < 0.3% among halo stars.

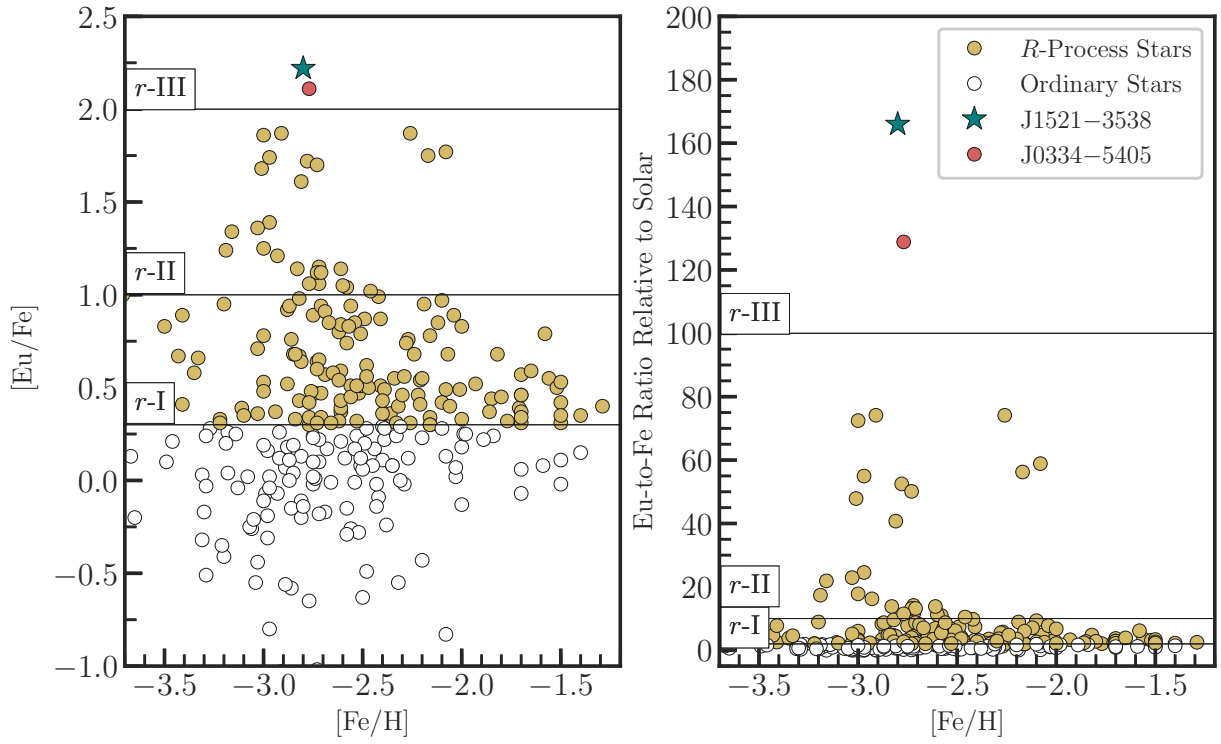

Figure 4. [Eu/Fe] and Eu-to-Fe ratio (relative to that of the Sun) plotted against [Fe/H] for J1521−3538, J0334−5405 (Ji et al. 2016a), and literature star data compiled from the JINAbase for metal-poor stars (Abohalima & Frebel 2018). *R*-I, *r*-II, and *r*-III boundaries are shown. References are Skúladóttir et al. (2015); Roederer et al. (2010); Burris et al. (2000); Roederer et al. (2014b,a); Hansen et al. (2015a); Barklem et al. (2005); Johnson & Bolte (2004); Jacobson et al. (2015); Cayrel et al. (2004); Hayek et al. (2009); Ji et al. (2016b); Johnson (2002); Placco et al. (2014); Roederer et al. (2008); Siqueira Mello et al. (2014, 2012); Cohen et al. (2006); Aoki et al. (2002b,a); Lai et al. (2008); Spite et al. (2014); Frebel et al. (2007); Honda et al. (2004, 2011); Jonsell et al. (2006); Placco et al. (2013); Ivans et al. (2003, 2006); Placco et al. (2015); Li et al. (2015); McWilliam et al. (1995); Cohen et al. (2003); Barbuy et al. (2005); Hollek et al. (2015); Masseron et al. (2006); Preston & Sneden (2001); Cui et al. (2013). See text for discussion.

5.2. *Kinematics*

The second data release from the Gaia mission (Lindegren et al. 2018) included measurements of the parallax ($\varpi = 0.4449 \pm 0.0614$ mas) and proper motions ($\mu_\alpha \cos\delta = -2.679 \pm 0.088$ mas yr^{-1}, $\mu_\delta = 24.135 \pm 0.062$ mas yr^{-1}) of J1521−3538. We use these data, plus the coordinates and the heliocentric radial velocity measured from our spectra, to compute the six-dimensional position and space velocity of J1521−3538. We follow the method described by Roederer et al. (2018a). That study adopted `MWPotential2014` for the Milky Way gravitational potential (Bovy 2015), computed orbits using the `Agama` code (Vasiliev 2019), and evaluated the specific energy and integrals of motion using the algorithm described by Binney (2012), as implemented in `Agama`. We resample the input quantities 10^3 times and recompute the kinematic properties from each resample. Table 5 lists the results of our calculations. The uncertainties quoted in Table 5 reflect statistical uncertainties only, and they do not account for systematic uncertainties in, e.g., the gravitational potential.

Our calculations indicate that J1521−3538 is on a bound, prograde orbit around the Galaxy, with a high eccentricity of 0.82. It is currently located relatively near its orbital pericenter ∼ 6 kpc from the Galactic center, and its eccentric orbit carries it more than 60 kpc from the Galactic center and 30 kpc above the Galactic plane. This presumably makes J1521−3538 an outer halo star. However, we note J1521−3538 has energy and actions that are distinct from any of the 35 highly r-process-enhanced stars whose kinematics were studied by Roederer et al. (2018a), so it is not likely to be affiliated with any of the groups identified in that study. All this, taken together with the low metallicity of J1521−3538, suggests it would have been born in a relatively low-mass dwarf galaxy (e.g., Kirby et al. 2013; Walker et al. 2016). The extreme r-process enhancement found in J1521−3538 may be a consequence of its birth in such a system if it underwent an early r-process event. A low-mass, low-density dwarf galaxy on an orbit similar to J1521−3538 would have been tidally disrupted long ago, and we suggest that this scenario led to the accretion of J1521−3538 by the Milky Way. Searches for other stars with similar kinematic properties may prove fruitful in the study of the nature and environment of the r-process (e.g., Yuan et al. 2020).

5.3. *Age Estimate for J1521−3538*

Stellar age estimates can be obtained if radioactive elements are present in the star and their abundances can be measured. The r-process produces thorium and uranium isotopes which have half-lives of 14 Gyr and 4.7 Gyr, respectively. Assuming that a single r-process event took place soon before the formation of the star, the abundances of such radioactive species can provide information on the age, provided that an initial production ratio is known. Theoretical r-process production ratios have been derived (Schatz et al. 2002; Hill et al. 2017) but remain uncertain given our incomplete understanding of the r-process itself and its astrophysical site of operation. Given these production ratios, the age estimate Δt can be calculated from

$$\Delta t = 46.78[\log\epsilon(\mathrm{Th/X_{initial}}) - \log\epsilon(\mathrm{Th/X_{now}})],$$

originally derived in Cayrel et al. (2001). Stellar abundance measurement uncertainties also have a significant impact on the resulting age. The statistical uncertainty for ages derived from Th (neglecting uncertainties in the initial production ratio) is given by

$$\sigma_{\Delta t} = 46.78\sqrt{\sigma^2_{\log\epsilon(\mathrm{Th})} + \sigma^2_{\log\epsilon(\mathrm{X})}},$$

where σ is the standard error in abundance.

Despite these challenges, we provide age estimates for J1521−3538 as derived from elemental abundances of Th with those of other heavy neutron-capture elements, such as Th/Eu. Since U only has an upper limit, it cannot be used to determine a meaningful age or limit. We employ production ratios derived from r-process waiting-point calculations (Schatz et al. 2002) and a high-entropy neutrino wind r-process model (Hill et al. 2017) to illustrate the impact of different theoretical assumptions. We caution that the results should be broadly interpreted only to show that J1521−3538 and other metal-poor stars are indeed ancient, in line with their low [Fe/H] values.

Table 6 list the results for various elemental abundance ratios involving Th for both sets of production ratios. We base our best age estimates on the abundance ratios Th/Ce, Th/Eu, Th/Dy, and Th/Er because they have the lowest statistical uncertainties, following Placco et al. (2017). Our analysis yields 12.5 Gyr using the Hill et al. (2017) production ratios and 8.9 Gyr when using the Schatz et al. (2002) values. We note that an age of 12.5 Gyr is more in line with expectations for a low-mass metal-poor star with [Fe/H] = −2.8 on the red horizontal branch. The other age of ∼ 9 Gyr may also be reasonable, given the uncertainties and the possibility that J1521−3538 was born in a low-mass dwarf galaxy.

Age uncertainties stemming from measurement uncertainties are listed in Table 6. Realistically, we adopt 5 Gyr for our age uncertainty. Uncertainties arising

Table 5. Kinematic properties of J1521−3538

Quantity	Description	Units	Value
D	Distance (inverse parallax)	kpc	$2.25^{+0.37}_{-0.29}$
$R_{\rm peri}$	Orbital pericentric radius	kpc	$5.95^{+0.20}_{-0.21}$
$R_{\rm apo}$	Orbital apocentric radius	kpc	$61.9^{+53.3}_{-20.2}$
$Z_{\rm max}$	Maximum height above or below the Galactic midplane	kpc	$32.0^{+20.9}_{-9.9}$
e	Eccentricity	...	$0.82^{+0.08}_{-0.08}$
V_R	Radial component of velocity in cylindrical coordinates	km s^{-1}	-121^{+10}_{-14}
V_ϕ	Azimuthal component of velocity in cylindrical coordinates[a]	km s^{-1}	326^{+18}_{-16}
V_z	Vertical component of velocity in cylindrical coordinates	km s^{-1}	249^{+35}_{-27}
$V_\perp$	$(V_R^2 + V_z^2)^{1/2}$	km s^{-1}	277^{+38}_{-29}
J_r	Radial action integral	kpc km s^{-1}	3150^{+3310}_{-1280}
J_ϕ	Azimuthal action integral[a]	kpc km s^{-1}	2000^{+20}_{-20}
J_z	Vertical action integral	kpc km s^{-1}	536^{+107}_{-85}
E	Specific orbital energy	(km s^{-1})^2	-51700^{+15800}_{-11000}

NOTE—The uncertainties reflect the range between the 50th percentile and the 84th (+) and 16th (−) percentiles of the distributions.

[a]Defined such that this quantity is positive for prograde rotation.

from the production ratios are difficult to quantify but can principally be regarded of order a few Gyr as well. Historically, just the Th/Eu alone has been used to date many r-process stars (e.g., Johnson & Bolte 2001; Hayek et al. 2009). Using just this ratio, we find 15 Gyr and 11 Gyr, respectively. Regardless of these uncertainties, the results for J1521−3538, as well as the ages of other r-process metal-poor stars, show that it remains important to find ways to characterize the progenitor r-process event and the birth site of each r-process star so that these events can be modeled individually. Given the actinide-boost phenomenon, it has become clear that perhaps not all r-process events produce the same amount of r-process elements. In this context, understanding the nature and origin of the actinide boost would also be crucial for obtaining more accurate stellar ages via cosmochronometry.

6. SUMMARY

The metal-poor horizontal branch star J1521−3538 was observed as part of efforts by the R-Process Alliance that aim to advance our understanding of the r-process by studying r-process-enhanced Galactic halo stars. We have discovered that J1521−3538 displays the strongest over-abundance of r-process elements observed in any r-process-enhanced star. The heavy-element abundance pattern from Sr to Th closely matches the scaled solar r-process pattern. A kinematic analysis of J1521−3538 shows it to be on a bound, prograde orbit around the Galaxy. This is distinct from other highly r-process-enhanced stars (Roederer et al. 2018a). Given that it also has a highly eccentric orbit, it was likely accreted from a low-mass dwarf galaxy. Other r-process stars with a similar kinematic signature may confirm this origin scenario.

Our detailed chemical abundance analysis shows that J1521−3538 is $\sim$ 12.5 Gyr and $\sim$ 8.9 Gyr old using the technique of cosmochronometry, which invokes abundance ratios of a radioactive element to other stable r-process elements. We used abundances from the Th II line at 4019 Å and lines of various r-process elements to derive these adopted ages. The two ages result from using two different sets of initial production ratios. The discrepancy highlights that the underlying r-process theory still requires fine tuning, or that the astrophysical site may play a significant role in the elemental yields of actinide-to-stable r-process element abundances. Hopefully, major facilities such as the Facility for Rare Isotope Beams (FRIB) will help to alleviate such discrepancies by providing fundamental nuclear species measurements

Table 6. Stellar age estimates for J1521−3538

Th/X	PR[i]	Age (Gyr)	PR[ii]	Age (Gyr)	$\sigma_{\Delta t}$ (Gyr)
Th/Ba	−1.058	13.19	...	...	6.29
Th/La	−0.362	16.74	−0.60	5.61	4.72
Th/Ce	−0.724	14.31	−0.79	11.22	4.72
Th/Pr	−0.313	6.40	−0.30	7.02	4.78
Th/Nd	−0.928	5.71	−0.91	6.55	4.72
Th/Sm	−0.796	−4.49	−0.61	4.21	4.81
Th/Eu	−0.240	14.97	−0.33	10.76	5.21
Th/Gd	−0.569	22.50	−0.81	11.23	4.97
Th/Tb	...	...	−0.12	5.14	6.62
Th/Dy	−0.827	10.43	−0.89	7.48	4.71
Th/Ho	−0.017	13.24	...	...	4.85
Th/Er	−0.592	10.20	−0.68	6.08	5.23
Th/Tm	0.155	6.31	0.12	4.68	5.71
Average		12.5		8.9	±5

[i] Production ratios from a high-entropy neutrino wind r-process model (Hill et al. 2017).

[ii] Production ratios from r-process waiting-point calculations (Schatz et al. 2002).

NOTE—Abundance ratios used for determining ages are Th/Ce, Th/Eu, Th/Dy, and Th/Er. Age averages are given ± the standard deviation of the age measurements included in the average, for illustrative purposes. $\sigma_{\Delta t}$ is the statistical error calculated from measurement uncertainties. The large spread in age estimates reflects measurement uncertainties and uncertainties in the theoretical models used to derive the production ratios.

that ultimately improve r-process predictions. Regardless, J1521−3538 is clearly an old star, which is supported by it being a low-mass metal-poor field red horizontal branch star. Hence, J1521−3538 adds to the growing inventory of highly r-process enhanced stars that will help to better characterize the nature of the r-process and its astrophysical site of operation.

We thank Chris Sneden for providing an up-to-date version of his neutron-capture line lists. M. C. acknowledges support from the MIT UROP program and the Heising-Simons Foundation. A. F. is partially supported by NSF-CAREER grant AST-1255160 and AST-1716251. This work benefited from support by the National Science Foundation under Grant No. PHY-1430152 (JINA Center for the Evolution of the Elements). A. P. J. is supported by NASA through Hubble Fellowship grant HST-HF2-51393.001 awarded by the Space Telescope Science Institute, which is operated by the Association of Universities for Research in Astronomy, Inc., for NASA, under contract NAS5-26555. I. U. R. acknowledges support from NSF grants AST 1613536 and AST 1815403. K. H. is supported by NASA-ATP award NNX15AK79G. T. C. B. acknowledges partial support from the Leverhulme Trust (UK), during his visiting professorship at the University Of Hull, when this paper was finished. This work made extensive use of NASA's Astrophysics Data System Bibliographic Services.

REFERENCES

Abbott, B. P., Abbott, R., Abbott, T. D., et al. 2017a, Physical Review Letters, 119, 161101

—. 2017b, ApJL, 848, L12

Abohalima, A., & Frebel, A. 2018, ApJS, 238, 36

Aoki, W., Beers, T. C., Christlieb, N., et al. 2007, ApJ, 655, 492

Aoki, W., Norris, J. E., Ryan, S. G., Beers, T. C., & Ando, H. 2002a, PASJ, 54, 933

Aoki, W., Ando, H., Honda, S., et al. 2002b, PASJ, 54, 427

Arcones, A., & Montes, F. 2011, ApJ, 731, 5

Arlandini, C., Käppeler, F., Wisshak, K., et al. 1999, ApJ, 525, 2

Asplund, M., Grevesse, N., Sauval, A. J., & Scott, P. 2009, ARA&A, 47, 481

Astropy Collaboration, Robitaille, T. P., Tollerud, E. J., et al. 2013, A&A, 558, A33

Barbuy, B., Spite, M., Spite, F., et al. 2005, A&A, 429, 1031

Barklem, P. S. 2018, A&A, 612, A90

Barklem, P. S., Christlieb, N., Beers, T. C., et al. 2005, A&A, 439, 129

Beers, T. C., & Christlieb, N. 2005, ARA&A, 43, 531

Beers, T. C., Norris, J. E., Placco, V. M., et al. 2014, ApJ, 794, 58

Beers, T. C., Placco, V. M., Carollo, D., et al. 2017, ApJ, 835, 81

Bernstein, R., Shectman, S. A., Gunnels, S. M., Mochnacki, S., & Athey, A. E. 2003, Proc. SPIE, 4841, 1694

Binney, J. 2012, MNRAS, 426, 1324

Bovy, J. 2015, ApJS, 216, 29

Brauer, K., Ji, A. P., Frebel, A., et al. 2019, ApJ, 871, 247

Burris, D. L., Pilachowski, C. A., Armandroff, T. E., et al. 2000, ApJ, 544, 302

Cain, M., Frebel, A., Gull, M., et al. 2018, ApJ, 864, 43

Casey, A. R. 2014, ArXiv e-prints, arXiv:1405.5968

Casey, A. R., & Schlaufman, K. C. 2017, ApJ, 850, 179

Casey, A. R., Hawkins, K., Hogg, D. W., et al. 2017, ApJ, 840, 59

Castelli, F., & Kurucz, R. L. 2004, ArXiv Astrophysics e-prints, astro-ph/0405087
Cayrel, R., Depagne, E., Spite, M., et al. 2004, A&A, 416, 1117
Cayrel, R., Hill, V., Beers, T.C., et al. 2001, Nature, 409, 691-692
Cohen, J. G., Christlieb, N., Qian, Y.-Z., & Wasserburg, G. J. 2003, ApJ, 588, 1082
Cohen, J. G., McWilliam, A., Shectman, S., et al. 2006, AJ, 132, 137
Coulter, D. A., Foley, R. J., Kilpatrick, C. D., et al. 2017, Science, 358, 1556
Cui, W. Y., Sivarani, T., & Christlieb, N. 2013, A&A, 558, A36
Dardelet, L., Ritter, C., Prado, P., et al. 2014, in XIII Nuclei in the Cosmos (NIC XIII), 145
Den Hartog, E. A., Ruffoni, M. P., Lawler, J. E., et al. 2014, ApJS, 215, 23
Drout, M. R., Piro, A. L., Shappee, B. J., et al. 2017, Science, 358, 1570
Ezzeddine, R., Frebel, A., & Plez, B. 2017, ApJ, 847, 142
Ezzeddine, R., Merle, T., & Plez, B. 2016, Astronomische Nachrichten, 337, 850
Ezzeddine, R., Merle, T., Plez, B., et al. 2018, A&A, 618, A141
Frebel, A. 2018, Annual Review of Nuclear and Particle Science, 68, 237
Frebel, A., Casey, A. R., Jacobson, H. R., & Yu, Q. 2013, ApJ, 769, 57
Frebel, A., Christlieb, N., Norris, J. E., et al. 2007, ApJL, 660, L117
Frebel, A., & Norris, J. E. 2015, ARA&A, 53, 631
Gaia Collaboration, Brown, A. G. A., Vallenari, A., et al. 2016a, A&A, 595, A2
Gaia Collaboration, Prusti, T., de Bruijne, J. H. J., et al. 2016b, A&A, 595, A1
Gull, M., Frebel, A., Cain, M. G., et al. 2018, ApJ, 862, 174
Hampel, M., Stancliffe, R. J., Lugaro, M., & Meyer, B. S. 2016, ApJ, 831, 171
Hansen, T., Hansen, C. J., Christlieb, N., et al. 2015a, ApJ, 807, 173
Hansen, T. T., Andersen, J., Nordström, B., et al. 2015b, A&A, 583, A49
Hansen, T. T., Holmbeck, E. M., Beers, T. C., et al. 2018, ApJ, 858, 92
Hayek, W., Wiesendahl, U., Christlieb, N., et al. 2009, A&A, 504, 511
Hill, V., Christlieb, N., Beers, T. C., et al. 2017, A&A, 607, A91
Hill, V., Plez, B., Cayrel, R., et al. 2002, A&A, 387, 560
Hollek, J. K., Frebel, A., Placco, V. M., et al. 2015, ApJ, 814, 121
Holmbeck, E. M., Beers, T. C., Roederer, I. U., et al. 2018, ApJL, 859, L24
Honda, S., Aoki, W., Beers, T. C., & Takada-Hidai, M. 2011, ApJ, 730, 77
Honda, S., Aoki, W., Kajino, T., et al. 2004, ApJ, 607, 474
Hunter, J. D. 2007, Computing in Science & Engineering, 9, 90
Ivans, I. I., Simmerer, J., Sneden, C., et al. 2006, ApJ, 645, 613
Ivans, I. I., Sneden, C., James, C. R., et al. 2003, ApJ, 592, 906
Jacobson, H. R., Keller, S., Frebel, A., et al. 2015, ApJ, 807, 171
Ji, A. P., & Frebel, A. 2018, ApJ, 856, 138
Ji, A. P., Frebel, A., Chiti, A., & Simon, J. D. 2016a, Nature, 531, 610
Ji, A. P., Frebel, A., Simon, J. D., & Chiti, A. 2016b, ApJ, 830, 93
Johnson, J. A. 2002, ApJS, 139, 219
Johnson, J. A., & Bolte, M. 2001, The Astrophysical Journal, 554, 888
—. 2004, ApJ, 605, 462
Jones, E., Oliphant, T., Peterson, P., et al. 2001, SciPy: Open source scientific tools for Python, ,
Jonsell, K., Barklem, P. S., Gustafsson, B., et al. 2006, A&A, 451, 651
Karakas, A. I., & Lattanzio, J. C. 2014, Publications of the Astronomical Society of Australia, 31, e030
Keeping, E. S. 1962, Introduction to Statistical Inference (Princeton, N.J., Van Nostrand)
Kelson, D. D. 2003, PASP, 115, 688
Kilpatrick, C. D., Foley, R. J., Kasen, D., et al. 2017, Science, 358, 1583
Kirby, E. N., Cohen, J. G., Guhathakurta, P., et al. 2013, ApJ, 779, 102
Kratz, K.-L., Farouqi, K., Pfeiffer, B., et al. 2007, ApJ, 662, 39
Kunder, A., Kordopatis, G., Steinmetz, M., et al. 2017, AJ, 153, 75
Kurucz, R. L. 1998, in IAU Symposium, Vol. 189, Fundamental Stellar Properties, ed. T. R. Bedding, A. J. Booth, & J. Davis, 217
Lai, D. K., Bolte, M., Johnson, J. A., et al. 2008, ApJ, 681, 1524
Li, H.-N., Zhao, G., Christlieb, N., et al. 2015, ApJ, 798, 110
Lind, K., Asplund, M., Barklem, P. S., & Belyaev, A. K. 2011, A&A, 528, A103

Lindegren, L., Hernández, J., Bombrun, A., et al. 2018, A&A, 616, A2

Marigo, P., Girardi, L., Bressan, A., et al. 2017, ApJ, 835, 77

Mashonkina, L., Christlieb, N., & Eriksson, K. 2014, Astronomy and Astrophysics, 569, A43

Masseron, T., van Eck, S., Famaey, B., et al. 2006, A&A, 455, 1059

Masseron, T., Plez, B., Van Eck, S., et al. 2014, A&A, 571, A47

McWilliam, A., Preston, G. W., Sneden, C., & Searle, L. 1995, AJ, 109, 2757

Meléndez, J., & Barbuy, B. 2009, A&A, 497, 611

Meléndez, J., Placco, V. M., Tucci-Maia, M., et al. 2016, A&A, 585, L5

Meyer, B. S., Mathews, G. J., Howard, W. M., Woosley, S. E., & Hoffman, R. D. 1992, ApJ, 399, 656

Nishimura, N., Takiwaki, T., & Thielemann, F.-K. 2015, ApJ, 810, 109

O'Brian, T. R., Wickliffe, M. E., Lawler, J. E., Whaling, J. W., & Brault, W. 1991, Journal of the Optical Society of America B Optical Physics, 8, 1185

Placco, V. M., Frebel, A., Beers, T. C., et al. 2013, ApJ, 770, 104

Placco, V. M., Frebel, A., Beers, T. C., & Stancliffe, R. J. 2014, ApJ, 797, 21

Placco, V. M., Beers, T. C., Ivans, I. I., et al. 2015, ApJ, 812, 109

Placco, V. M., Holmbeck, E. M., Frebel, A., et al. 2017, ApJ, 844, 18

Placco, V. M., Beers, T. C., Santucci, R. M., et al. 2018, AJ, 155, 256

Preston, G. W., & Sneden, C. 2001, AJ, 122, 1545

Preston, G. W., Sneden, C., Thompson, I. B., Shectman, S. A., & Burley, G. S. 2006, AJ, 132, 85

Roederer, I. U., Cowan, J. J., Preston, G. W., et al. 2014a, MNRAS, 445, 2970

Roederer, I. U., Hattori, K., & Valluri, M. 2018a, AJ, 156, 179

Roederer, I. U., Mateo, M., Bailey, J. I., et al. 2016, MNRAS, 455, 2417

Roederer, I. U., Preston, G. W., Thompson, I. B., et al. 2014b, AJ, 147, 136

Roederer, I. U., Sakari, C. M., Placco, V. M., et al. 2018b, ApJ, 865, 129

Roederer, I. U., Sneden, C., Thompson, I. B., Preston, G. W., & Shectman, S. A. 2010, ApJ, 711, 573

Roederer, I. U., Frebel, A., Shetrone, M. D., et al. 2008, ApJ, 679, 1549

Ruffoni, M. P., Den Hartog, E. A., Lawler, J. E., et al. 2014, MNRAS, 441, 3127

Sakari, C. M., Placco, V. M., Hansen, T., et al. 2018, ApJL, 854, L20

Sakari, C. M., Roederer, I. U., Placco, V. M., et al. 2019, ApJ, 874, 148

Schatz, H., Toenjes, R., Pfeiffer, B., et al. 2002, ApJ, 579, 626

Shappee, B. J., Simon, J. D., Drout, M. R., et al. 2017, Science, 358, 1574

Siegel, D. M., Barnes, J., & Metzger, B. D. 2019, Nature, 569, 241

Siqueira Mello, C., Barbuy, B., Spite, M., & Spite, F. 2012, A&A, 548, A42

Siqueira Mello, C., Hill, V., Barbuy, B., et al. 2014, A&A, 565, A93

Skúladóttir, Á., Tolstoy, E., Salvadori, S., et al. 2015, A&A, 574, A129

Sneden, C., Cowan, J. J., & Gallino, R. 2008, ARA&A, 46, 241

Sneden, C., Cowan, J. J., Kobayashi, C., et al. 2016, ApJ, 817, 53

Sneden, C., Lawler, J. E., Cowan, J. J., Ivans, I. I., & Den Hartog, E. A. 2009, ApJS, 182, 80

Sneden, C., Lucatello, S., Ram, R. S., Brooke, J. S. A., & Bernath, P. 2014, ApJS, 214, 26

Sneden, C., McWilliam, A., Preston, G. W., et al. 1996, ApJ, 467, 819

Sneden, C. A. 1973, PhD thesis, The University of Texas at Austin.

Sobeck, J. S., Kraft, R. P., Sneden, C., et al. 2011, AJ, 141, 175

Spite, M., Spite, F., Bonifacio, P., et al. 2014, A&A, 571, A40

Surman, R., McLaughlin, G. C., & Hix, W. R. 2006, The Astrophysical Journal, 643, 1057

Tody, D. 1986, in Proc. SPIE, Vol. 627, Instrumentation in astronomy VI, ed. D. L. Crawford, 733

Tody, D. 1993, in Astronomical Society of the Pacific Conference Series, Vol. 52, Astronomical Data Analysis Software and Systems II, ed. R. J. Hanisch, R. J. V. Brissenden, & J. Barnes, 173

Travaglio, C., Gallino, R., Arnone, E., et al. 2004, ApJ, 601, 864

Truran, J. W., Cowan, J. J., Pilachowski, C. A., & Sneden, C. 2002, PASP, 114, 1293

van der Walt, S., Colbert, S. C., & Varoquaux, G. 2011, Computing in Science & Engineering, 13, 22

Vasiliev, E. 2019, MNRAS, 482, 1525

Walker, M. G., Mateo, M., Olszewski, E. W., et al. 2016, ApJ, 819, 53

Wanajo, S. 2013, ApJL, 770, L22

Wanajo, S., & Ishimaru, Y. 2006, Nuclear Physics A, 777, 676

Wanajo, S., Kajino, T., Mathews, G. J., & Otsuki, K. 2001, ApJ, 554, 578

Woosley, S. E., & Hoffman, R. D. 1992, ApJ, 395, 202

Yong, D., Norris, J. E., Bessell, M. S., et al. 2013, ApJ, 762, 26

Yuan, Z., Myeong, G. C., Beers, T. C., et al. 2020, ApJ, 891, 1

Facilities: Magellan:Clay (MIKE), Gemini:South (GMOS)

Software: MOOG (Sneden 1973; Sobeck et al. 2011), MIKE Carnegie Python Pipeline (Kelson 2003), IRAF (Tody 1986, 1993), NumPy (van der Walt et al. 2011), SciPy (Jones et al. 2001), Matplotlib (Hunter 2007), Astropy (Astropy Collaboratio 2013)

Table 7. Line list and derived abundances for J1521−3538

Element	λ [Å]	EP [eV]	log *gf*	EW [mÅ]	log ϵ(X)
CH	4312	...	...	syn	6.20
Na I	5889.95	0.00	0.11	121.0	3.69
Na I	5895.92	0.00	−0.19	89.7	3.54
Mg I	3986.75	4.35	−1.03	12.9	5.25
Mg I	4057.51	4.35	−0.89	11.0	5.03
Mg I	4167.27	4.35	−0.71	23.2	5.22
Mg I	4702.99	4.33	−0.38	35.9	5.10
Mg I	5528.40	4.34	−0.50	32.7	5.16
Mg I	5711.09	4.34	−1.72	3.4	5.30
Al I	3944.00	0.00	−0.64	syn	2.93
Al I	3961.52	0.01	−0.34	79.4	2.88
Si I	3906.52	1.91	−1.09	syn	4.79
Ca I	4283.01	1.89	−0.22	20.2	3.86
Ca I	4318.65	1.89	−0.21	21.8	3.89
Ca I	4425.44	1.88	−0.36	13.8	3.79
Ca I	4434.96	1.89	−0.01	27.9	3.81
Ca I	4454.78	1.90	0.26	61.1	4.07
Ca I	4455.89	1.90	−0.53	9.7	3.81
Ca I	5265.56	2.52	−0.26	11.0	4.17
Ca I	5594.47	2.52	0.10	16.1	3.99
Ca I	5598.49	2.52	−0.09	6.1	3.71
Ca I	5857.45	2.93	0.23	5.5	3.72
Ca I	6102.72	1.88	−0.79	7.8	3.90
Ca I	6122.22	1.89	−0.32	18.5	3.85
Ca I	6162.17	1.90	−0.09	28.9	3.87
Ca I	6439.07	2.52	0.47	20.1	3.71
Sc II	4246.81	0.32	0.24	107.4	0.56
Sc II	4314.08	0.62	−0.10	52.1	0.40
Sc II	4324.98	0.59	−0.44	29.2	0.36
Sc II	4400.38	0.60	−0.54	26.3	0.41
Sc II	4415.54	0.59	−0.67	22.9	0.46
Sc II	5031.01	1.36	−0.40	8.0	0.39
Sc II	5526.77	1.77	0.02	7.6	0.32
Sc II	5657.89	1.51	−0.60	5.6	0.54
Ti I	3989.76	0.02	−0.13	19.8	2.68
Ti I	3998.64	0.05	0.02	13.5	2.37
Ti I	4533.24	0.85	0.54	11.1	2.49
Ti I	4534.78	0.83	0.35	9.8	2.61
Ti I	4981.73	0.85	0.57	9.8	2.38
Ti I	4991.07	0.83	0.45	16.3	2.73
Ti I	4999.50	0.82	0.32	15.3	2.82
Ti I	5007.21	0.82	0.17	9.4	2.73
Ti II	3489.74	0.14	−2.00	39.7	2.29
Ti II	3491.05	0.11	−1.10	96.0	2.40
Ti II	3913.46	1.11	−0.36	124.2	2.76
Ti II	4025.13	0.61	−2.11	23.9	2.35
Ti II	4028.34	1.89	−0.92	33.0	2.59
Ti II	4053.82	1.89	−1.07	10.7	2.16
Ti II	4163.64	2.59	−0.13	34.4	2.48
Ti II	4290.22	1.16	−0.87	71.3	2.35
Ti II	4300.04	1.18	−0.46	102.1	2.41
Ti II	4337.91	1.08	−0.96	67.9	2.31

Table 7 continued

Table 7 *(continued)*

Element	λ [Å]	EP [eV]	log *gf*	EW [mÅ]	log ϵ(X)
Ti II	4394.06	1.22	−1.77	15.9	2.37
Ti II	4395.03	1.08	−0.54	112.7	2.56
Ti II	4395.84	1.24	−1.93	13.2	2.46
Ti II	4399.77	1.24	−1.19	41.7	2.33
Ti II	4417.71	1.17	−1.19	56.0	2.45
Ti II	4418.33	1.24	−1.99	13.3	2.51
Ti II	4441.73	1.18	−2.41	7.1	2.58
Ti II	4443.80	1.08	−0.71	97.2	2.46
Ti II	4450.48	1.08	−1.52	37.8	2.44
Ti II	4464.45	1.16	−1.81	19.1	2.43
Ti II	4468.49	1.13	−0.63	103.3	2.53
Ti II	4501.27	1.11	−0.77	90.2	2.44
Ti II	4533.96	1.24	−0.53	99.2	2.46
Ti II	4563.77	1.22	−0.96	78.1	2.56
Ti II	4571.97	1.57	−0.31	96.3	2.52
Ti II	4589.91	1.24	−1.79	20.3	2.51
Ti II	4657.20	1.24	−2.29	8.2	2.58
Ti II	4708.66	1.24	−2.35	4.6	2.37
Ti II	4779.98	2.05	−1.37	16.5	2.77
Ti II	4798.53	1.08	−2.68	5.2	2.59
Ti II	4805.09	2.06	−1.10	20.4	2.62
Ti II	5129.16	1.89	−1.34	12.4	2.43
Ti II	5185.90	1.89	−1.41	8.8	2.34
Ti II	5188.69	1.58	−1.05	31.9	2.31
Ti II	5226.54	1.57	−1.26	20.7	2.28
Ti II	5336.79	1.58	−1.60	14.8	2.46
Ti II	5381.02	1.56	−1.97	13.1	2.75
V II	3951.41	1.48	−0.78	syn	1.31
V II	4005.71	1.82	−1.52	syn	1.32
Cr I	3578.68	0.00	0.42	74.9	2.56
Cr I	4254.33	0.00	−0.09	65.4	2.54
Cr I	4274.80	0.00	−0.22	58.4	2.57
Cr I	4289.72	0.00	−0.37	52.7	2.64
Cr I	5206.04	0.94	0.02	28.7	2.73
Cr I	5208.42	0.94	0.17	35.2	2.70
Cr I	5409.77	1.03	−0.67	4.6	2.61
Mn I	4030.75	0.00	−0.50	syn	1.92
Mn I	4033.06	0.00	−0.65	syn	1.86
Mn I	4034.48	0.00	−0.84	syn	1.81
Mn I	4041.35	2.11	0.28	syn	1.98
Fe I	3417.84	2.22	−0.68	22.6	4.55
Fe I	3476.70	0.12	−1.51	104.1	4.96
Fe I	3497.84	0.11	−1.55	95.8	4.78
Fe I	3521.26	0.91	−0.99	61.4	4.29
Fe I	3558.52	0.99	−0.63	107.9	5.03
Fe I	3608.86	1.01	−0.09	114.1	4.67
Fe I	3610.16	2.81	0.12	38.8	4.65
Fe I	3709.25	0.91	−0.62	110.1	4.50
Fe I	3727.62	0.96	−0.61	117.8	4.69
Fe I	3742.62	2.94	−0.81	13.5	4.88
Fe I	3765.54	3.24	0.48	55.6	4.70
Fe I	3787.88	1.01	−0.84	100.5	4.58
Fe I	3790.09	0.99	−1.74	39.4	4.51
Fe I	3795.00	0.99	−0.74	108.5	4.63
Fe I	3805.34	3.30	0.31	66.3	5.07
Fe I	3812.97	0.96	−1.05	106.4	4.86
Fe I	3816.34	2.20	−1.20	9.2	4.37
Fe I	3841.05	1.61	−0.04	113.9	4.64
Fe I	3846.80	3.25	−0.02	28.9	4.77
Fe I	3849.97	1.01	−0.86	108.1	4.75
Fe I	3865.52	1.01	−0.95	103.5	4.74

Table 7 continued

Table 7 *(continued)*

Element	λ [Å]	EP [eV]	log *gf*	EW [mÅ]	log ϵ(X)
Fe I	3867.22	3.02	−0.45	16.2	4.67
Fe I	3872.50	0.99	−0.89	102.5	4.63
Fe I	3878.02	0.96	−0.90	107.7	4.71
Fe I	3887.05	0.91	−1.14	81.1	4.43
Fe I	3895.66	0.11	−1.67	112.8	4.75
Fe I	3898.01	1.01	−2.04	39.6	4.82
Fe I	3902.95	1.56	−0.44	93.7	4.58
Fe I	3917.18	0.99	−2.15	23.5	4.62
Fe I	3920.26	0.12	−1.73	108.5	4.73
Fe I	3940.88	0.96	−2.60	11.7	4.68
Fe I	3949.95	2.18	−1.25	10.9	4.48
Fe I	3977.74	2.20	−1.12	19.2	4.64
Fe I	4005.24	1.56	−0.58	92.9	4.68
Fe I	4009.71	2.22	−1.25	14.6	4.65
Fe I	4014.53	3.05	−0.59	21.2	4.97
Fe I	4067.98	3.21	−0.53	15.0	4.88
Fe I	4071.74	1.61	−0.01	120.8	4.68
Fe I	4076.63	3.21	−0.59	19.8	5.08
Fe I	4084.49	3.33	−0.54	7.3	4.66
Fe I	4132.06	1.61	−0.68	96.1	4.86
Fe I	4132.90	2.85	−1.01	8.6	4.75
Fe I	4134.68	2.83	−0.65	19.4	4.77
Fe I	4137.00	3.42	−0.45	10.3	4.81
Fe I	4143.87	1.56	−0.51	97.5	4.67
Fe I	4147.67	1.48	−2.07	13.5	4.71
Fe I	4153.90	3.40	−0.28	9.9	4.61
Fe I	4156.80	2.83	−0.81	13.1	4.73
Fe I	4157.78	3.42	−0.40	10.9	4.79
Fe I	4172.75	0.96	−3.02	5.2	4.70
Fe I	4175.64	2.85	−0.83	21.2	5.00
Fe I	4181.76	2.83	−0.37	29.3	4.70
Fe I	4184.89	2.83	−0.87	12.0	4.75
Fe I	4187.04	2.45	−0.56	39.2	4.70
Fe I	4187.80	2.42	−0.51	37.1	4.59
Fe I	4191.43	2.47	−0.67	33.7	4.74
Fe I	4199.10	3.05	0.16	43.0	4.62
Fe I	4202.03	1.49	−0.69	92.7	4.68
Fe I	4216.18	0.00	−3.36	16.8	4.64
Fe I	4217.55	3.43	−0.48	11.5	4.91
Fe I	4222.21	2.45	−0.91	17.7	4.61
Fe I	4227.43	3.33	0.27	41.3	4.75
Fe I	4233.60	2.48	−0.60	30.0	4.61
Fe I	4238.81	3.40	−0.23	16.1	4.79
Fe I	4250.12	2.47	−0.38	45.3	4.63
Fe I	4250.79	1.56	−0.71	86.3	4.67
Fe I	4260.47	2.40	0.08	80.9	4.62
Fe I	4271.15	2.45	−0.34	48.3	4.61
Fe I	4271.76	1.49	−0.17	130.9	4.89
Fe I	4282.40	2.18	−0.78	46.6	4.76
Fe I	4325.76	1.61	0.01	133.0	4.87
Fe I	4352.73	2.22	−1.29	15.8	4.70
Fe I	4375.93	0.00	−3.00	37.7	4.71
Fe I	4404.75	1.56	−0.15	127.4	4.84
Fe I	4415.12	1.61	−0.62	90.0	4.66
Fe I	4427.31	0.05	−2.92	37.2	4.67
Fe I	4442.34	2.20	−1.23	18.4	4.69
Fe I	4447.72	2.22	−1.34	12.5	4.63
Fe I	4459.12	2.18	−1.28	15.8	4.64
Fe I	4461.65	0.09	−3.19	22.0	4.68
Fe I	4466.55	2.83	−0.60	19.4	4.69
Fe I	4476.02	2.85	−0.82	13.0	4.73

Table 7 continued

Table 7 *(continued)*

Element	λ [Å]	EP [eV]	log gf	EW [mÅ]	log ϵ(X)
Fe I	4489.74	0.12	−3.90	2.4	4.39
Fe I	4494.56	2.20	−1.14	20.5	4.66
Fe I	4528.61	2.18	−0.82	44.2	4.75
Fe I	4531.15	1.48	−2.10	12.6	4.67
Fe I	4602.94	1.49	−2.21	8.8	4.61
Fe I	4736.77	3.21	−0.67	9.2	4.75
Fe I	4871.32	2.87	−0.34	23.0	4.54
Fe I	4872.14	2.88	−0.57	16.7	4.62
Fe I	4890.76	2.88	−0.38	30.7	4.75
Fe I	4891.49	2.85	−0.11	37.2	4.57
Fe I	4903.31	2.88	−0.89	8.7	4.62
Fe I	4918.99	2.85	−0.34	23.9	4.54
Fe I	4920.50	2.83	0.07	55.9	4.64
Fe I	4938.81	2.88	−1.08	4.6	4.51
Fe I	4994.13	0.92	−2.97	12.1	4.94
Fe I	5001.87	3.88	−0.01	10.0	4.76
Fe I	5006.12	2.83	−0.61	16.7	4.61
Fe I	5012.07	0.86	−2.64	17.4	4.73
Fe I	5041.07	0.96	−3.09	9.1	4.96
Fe I	5049.82	2.28	−1.35	13.0	4.69
Fe I	5079.74	0.99	−3.25	7.4	5.05
Fe I	5083.34	0.96	−2.84	6.2	4.54
Fe I	5110.41	0.00	−3.76	13.3	4.86
Fe I	5123.72	1.01	−3.06	13.9	5.18
Fe I	5133.69	4.17	0.36	9.8	4.66
Fe I	5151.91	1.01	−3.32	3.6	4.82
Fe I	5162.27	4.18	0.02	5.9	4.76
Fe I	5171.60	1.49	−1.72	23.0	4.56
Fe I	5191.45	3.04	−0.55	34.2	5.13
Fe I	5227.19	1.56	−1.23	53.7	4.65
Fe I	5232.94	2.94	−0.06	38.5	4.61
Fe I	5266.56	3.00	−0.39	18.7	4.59
Fe I	5269.54	0.86	−1.33	96.6	4.67
Fe I	5281.79	3.04	−0.83	9.1	4.73
Fe I	5302.30	3.28	−0.73	10.2	4.91
Fe I	5324.18	3.21	−0.11	22.1	4.60
Fe I	5328.04	0.92	−1.47	83.2	4.65
Fe I	5328.53	1.56	−1.85	25.7	4.81
Fe I	5339.93	3.27	−0.63	5.8	4.54
Fe I	5364.87	4.45	0.23	4.6	4.70
Fe I	5367.47	4.42	0.44	6.2	4.59
Fe I	5369.96	4.37	0.54	11.8	4.75
Fe I	5371.49	0.96	−1.64	70.4	4.69
Fe I	5383.37	4.31	0.65	16.1	4.74
Fe I	5393.17	3.24	−0.91	7.7	4.92
Fe I	5397.13	0.92	−1.98	44.9	4.64
Fe I	5405.77	0.99	−1.85	48.4	4.63
Fe I	5410.91	4.47	0.40	7.6	4.77
Fe I	5415.20	4.39	0.64	13.1	4.71
Fe I	5424.07	4.32	0.52	14.6	4.82
Fe I	5429.70	0.96	−1.88	50.9	4.67
Fe I	5434.52	1.01	−2.13	30.0	4.63
Fe I	5446.92	0.99	−1.91	46.2	4.66
Fe I	5497.52	1.01	−2.83	14.5	4.95
Fe I	5506.78	0.99	−2.79	12.9	4.83
Fe I	5572.84	3.40	−0.28	12.8	4.67
Fe I	5586.76	3.37	−0.11	14.8	4.54
Fe I	5615.64	3.33	0.04	21.4	4.54
Fe I	5624.54	3.42	−0.76	3.4	4.56
Fe I	5709.38	3.37	−1.01	5.2	4.95
Fe I	6065.48	2.61	−1.41	5.9	4.66

Table 7 continued

Table 7 *(continued)*

Element	λ [Å]	EP [eV]	log *gf*	EW [mÅ]	log ϵ(X)
Fe I	6136.61	2.45	−1.41	6.8	4.57
Fe I	6191.56	2.43	−1.42	7.7	4.61
Fe I	6230.72	2.56	−1.28	6.7	4.53
Fe I	6252.56	2.40	−1.69	6.3	4.76
Fe I	6393.60	2.43	−1.58	4.7	4.54
Fe I	6400.00	3.60	−0.27	8.7	4.65
Fe I	6592.91	2.73	−1.47	7.9	4.95
Fe I	6677.99	2.69	−1.42	6.0	4.73
Fe I	7495.07	4.22	−0.10	4.7	4.76
Fe I	8387.77	2.17	−1.51	18.6	4.76
Fe I	8688.62	2.17	−1.20	50.9	5.01
Fe II	4178.86	2.58	−2.51	31.7	4.72
Fe II	4233.17	2.58	−1.97	70.7	4.75
Fe II	4416.82	2.78	−2.65	24.0	4.88
Fe II	4489.19	2.83	−2.96	10.2	4.80
Fe II	4491.41	2.86	−2.71	13.8	4.73
Fe II	4508.28	2.86	−2.44	25.4	4.77
Fe II	4515.34	2.84	−2.60	20.9	4.81
Fe II	4520.22	2.81	−2.65	18.6	4.77
Fe II	4555.89	2.83	−2.40	Fe I	4.71
Fe II	4576.34	2.84	−2.95	8.4	4.71
Fe II	4582.84	2.84	−3.18	4.6	4.67
Fe II	4583.84	2.81	−1.93	60.6	4.77
Fe II	4620.52	2.83	−3.21	3.5	4.57
Fe II	4923.93	2.89	−1.26	91.7	4.60
Fe II	5018.45	2.89	−1.10	102.9	4.61
Fe II	5169.03	2.89	−1.00	122.8	4.85
Fe II	5197.58	3.23	−2.22	16.4	4.65
Fe II	5234.63	3.22	−2.18	24.5	4.81
Fe II	5276.00	3.20	−2.01	26.7	4.67
Fe II	5316.62	3.15	−1.87	45.1	4.79
Fe II	5534.83	3.25	−2.75	4.1	4.54
Co I	3873.12	0.43	−0.66	syn	2.32
Co I	3995.31	0.92	−0.22	syn	2.29
Co I	4020.83	3.66	−0.96	syn	2.43
Co I	4121.31	0.92	−0.32	syn	2.23
Ni I	3423.71	0.21	−0.71	73.6	3.23
Ni I	3433.56	0.03	−0.67	97.5	3.55
Ni I	3452.89	0.11	−0.90	88.0	3.63
Ni I	3472.54	0.11	−0.79	76.5	3.26
Ni I	3483.78	0.28	−1.11	48.7	3.23
Ni I	3492.96	0.11	−0.27	94.7	3.15
Ni I	3500.85	0.17	−1.27	53.9	3.36
Ni I	3519.76	0.28	−1.44	51.0	3.59
Ni I	3566.37	0.42	−0.25	84.3	3.18
Ni I	3597.70	0.21	−1.10	59.6	3.33
Ni I	3783.53	0.42	−1.40	57.6	3.55
Ni I	3807.14	0.42	−1.23	63.6	3.46
Ni I	3858.30	0.42	−0.96	81.8	3.46
Ni I	5476.90	1.82	−0.78	21.8	3.58
Zn I	4810.53	4.08	−0.15	2.7	1.80
Sr II	4161.79	−0.60	2.94	syn	1.24
Y II	3611.04	0.13	0.11	syn	0.53
Y II	3710.29	0.18	0.46	syn	0.66
Y II	4398.01	0.13	−1.00	syn	0.45
Y II	4682.73	0.41	−1.51	syn	0.42
Y II	4854.87	0.99	−0.38	syn	0.45
Y II	4883.68	1.08	0.07	syn	0.53
Y II	4900.11	1.03	−0.09	syn	0.35
Y II	5087.42	1.08	−0.17	syn	0.42
Y II	5199.11	0.99	−1.36	syn	0.26

Table 7 continued

Table 7 *(continued)*

Element	λ [Å]	EP [eV]	log *gf*	EW [mÅ]	log ϵ(X)
Y II	5205.73	1.03	−1.34	syn	0.39
Zr II	3479.02	0.53	−0.69	syn	0.88
Zr II	3499.57	0.41	−0.81	syn	1.02
Zr II	4050.33	0.71	−1.00	syn	1.14
Zr II	4149.20	0.80	−0.03	syn	1.21
Zr II	4161.21	0.71	−0.72	syn	1.32
Zr II	4208.99	0.71	−0.46	syn	1.09
Zr II	4317.32	0.71	−1.38	syn	1.18
Zr II	4613.95	0.97	−1.52	syn	1.22
Ru I	3728.03	0.00	0.27	syn	0.89
Ba II	4130.65	2.72	0.68	syn	0.63
Ba II	5853.69	0.60	−0.91	syn	0.84
La II	3794.77	0.24	0.21	syn	0.00
La II	3849.01	0.00	−0.45	syn	0.13
La II	3929.21	0.17	−0.32	syn	0.02
La II	3949.10	0.00	0.49	syn	0.04
La II	3988.51	0.40	0.21	syn	0.10
La II	4086.71	0.00	−0.07	syn	0.19
La II	4123.22	0.32	0.13	syn	0.09
La II	4141.72	0.40	−0.66	syn	0.06
La II	4322.51	0.17	−0.93	syn	0.17
La II	4333.75	0.17	−0.06	syn	0.10
La II	4429.91	0.23	−0.35	syn	0.09
La II	4526.12	0.77	−0.59	syn	0.05
La II	4574.88	0.17	−1.08	syn	0.08
La II	4662.51	0.00	−1.24	syn	0.22
La II	4748.73	0.93	−0.54	syn	0.12
La II	4921.78	0.24	−0.45	syn	0.15
La II	5114.56	0.23	−1.03	syn	0.25
La II	5122.99	0.32	−0.85	syn	0.19
Ce II	3942.15	0.00	−0.22	31.4	0.58
Ce II	3942.74	0.86	0.69	26.4	0.42
Ce II	4083.22	0.70	0.27	17.2	0.45
Ce II	4120.83	0.32	−0.37	10.3	0.46
Ce II	4127.36	0.68	0.31	16.4	0.36
Ce II	4137.65	0.52	0.40	32.4	0.47
Ce II	4142.40	0.70	0.22	14.1	0.39
Ce II	4145.00	0.70	0.10	12.1	0.43
Ce II	4222.60	0.12	−0.15	23.3	0.43
Ce II	4364.65	0.49	−0.17	7.7	0.27
Ce II	4382.16	0.68	0.13	11.5	0.34
Ce II	4399.20	0.33	−0.44	6.0	0.25
Ce II	4449.33	0.61	0.04	13.2	0.41
Ce II	4486.91	0.29	−0.18	14.0	0.35
Ce II	4523.07	0.52	−0.08	22.6	0.71
Ce II	4560.28	0.91	0.18	12.4	0.54
Ce II	4560.96	0.68	−0.26	6.1	0.42
Ce II	4562.36	0.48	0.21	23.4	0.39
Ce II	4593.93	0.70	0.07	13.3	0.47
Ce II	4628.16	0.52	0.14	19.7	0.41
Pr II	4062.81	0.42	0.33	syn	−0.06
Pr II	4143.13	0.37	0.60	syn	−0.16
Pr II	4164.16	0.20	0.17	syn	−0.25
Pr II	4179.39	0.20	0.48	syn	−0.21
Pr II	4189.48	0.37	0.38	syn	−0.18
Pr II	4222.95	0.06	0.27	syn	−0.17
Pr II	4408.82	0.00	0.18	syn	−0.22
Pr II	4449.83	0.20	−0.26	syn	0.02
Nd II	3784.24	0.38	0.15	28.8	0.38
Nd II	3927.10	0.18	−0.59	10.9	0.41
Nd II	3990.10	0.47	0.13	31.0	0.51

Table 7 continued

Table 7 *(continued)*

Element	λ [Å]	EP [eV]	log *gf*	EW [mÅ]	log ϵ(X)
Nd II	4007.43	0.47	−0.40	9.8	0.45
Nd II	4012.70	0.00	−0.60	18.5	0.49
Nd II	4021.33	0.32	−0.10	20.5	0.36
Nd II	4023.00	0.56	0.04	27.2	0.61
Nd II	4043.59	0.32	−0.71	6.2	0.39
Nd II	4051.14	0.38	−0.30	14.6	0.44
Nd II	4059.95	0.20	−0.52	10.3	0.32
Nd II	4061.08	0.47	0.55	54.7	0.46
Nd II	4069.26	0.06	−0.57	15.5	0.42
Nd II	4109.45	0.32	0.35	50.6	0.44
Nd II	4133.35	0.32	−0.49	10.5	0.41
Nd II	4135.32	0.63	−0.07	21.0	0.64
Nd II	4211.29	0.20	−0.86	6.1	0.40
Nd II	4232.37	0.06	−0.47	20.7	0.46
Nd II	4284.51	0.63	−0.17	11.7	0.43
Nd II	4351.28	0.18	−0.61	15.0	0.54
Nd II	4358.16	0.32	−0.16	21.0	0.39
Nd II	4368.63	0.06	−0.81	9.2	0.39
Nd II	4385.66	0.20	−0.30	22.5	0.45
Nd II	4400.82	0.06	−0.60	10.1	0.21
Nd II	4446.38	0.20	−0.35	18.1	0.38
Nd II	4462.98	0.56	0.04	22.0	0.45
Nd II	4465.06	0.00	−1.36	4.2	0.51
Nd II	4501.81	0.20	−0.69	9.8	0.42
Nd II	4542.60	0.74	−0.28	7.0	0.39
Nd II	4563.22	0.18	−0.88	10.3	0.61
Nd II	4567.61	0.20	−1.31	3.7	0.59
Nd II	4645.76	0.56	−0.76	3.7	0.39
Nd II	4706.54	0.00	−0.71	14.0	0.39
Nd II	4709.72	0.18	−0.97	7.6	0.54
Nd II	4715.59	0.20	−0.90	5.3	0.33
Nd II	4820.34	0.20	−0.92	8.3	0.55
Nd II	4825.48	0.18	−0.42	16.6	0.35
Nd II	4914.38	0.38	−0.70	6.4	0.38
Nd II	4959.12	0.06	−0.80	10.3	0.38
Nd II	5092.79	0.38	−0.61	14.1	0.64
Nd II	5130.59	1.30	0.45	14.5	0.52
Nd II	5234.19	0.55	−0.51	10.6	0.57
Nd II	5249.58	0.97	0.20	12.6	0.37
Nd II	5255.51	0.20	−0.67	9.8	0.34
Nd II	5273.43	0.68	−0.18	12.8	0.46
Nd II	5293.16	0.82	0.10	17.2	0.47
Nd II	5319.81	0.55	−0.14	22.7	0.57
Sm II	3568.89	0.00	−2.15	syn	0.11
Sm II	4065.01	0.04	−2.34	syn	−0.07
Sm II	4511.83	0.18	−0.82	syn	0.18
Sm II	4519.63	0.54	−0.35	syn	0.10
Sm II	4537.94	0.49	−0.48	syn	0.10
Sm II	4554.44	0.10	−1.25	syn	0.14
Sm II	4591.81	0.18	−1.12	syn	0.13
Sm II	4595.28	0.49	−0.50	syn	0.12
Sm II	4595.28	0.49	−0.50	syn	0.12
Sm II	4605.17	0.04	−1.39	syn	−0.02
Sm II	4686.19	0.04	−1.15	syn	0.15
Sm II	4719.84	0.04	−1.24	syn	0.05
Sm II	4745.68	0.10	−0.93	syn	0.14
Eu II	3724.93	0.00	−0.09	syn	−0.11
Eu II	3819.67	0.00	0.51	syn	−0.04
Eu II	3907.11	0.21	0.17	syn	−0.12
Eu II	4129.72	0.00	0.22	syn	−0.11
Eu II	4205.04	0.00	0.21	syn	−0.16

Table 7 continued

Table 7 *(continued)*

Element	λ [Å]	EP [eV]	log *gf*	EW [mÅ]	log ϵ(X)
Eu II	6645.06	1.38	0.12	syn	0.04
Eu II	7217.56	1.23	−0.35	syn	0.22
Gd II	3768.40	0.08	0.21	51.3	0.22
Gd II	3894.69	0.00	−0.58	29.6	0.56
Gd II	4037.32	0.66	−0.11	14.8	0.36
Gd II	4049.42	0.66	−0.08	14.6	0.32
Gd II	4049.85	0.99	0.49	30.5	0.47
Gd II	4191.07	0.43	−0.48	14.4	0.47
Gd II	4251.73	0.38	−0.22	24.1	0.42
Gd II	4316.05	0.66	−0.45	12.3	0.58
Gd II	4438.25	0.66	−0.82	6.3	0.63
Tb II	3568.45	0.00	0.36	syn	−0.42
Tb II	3658.89	0.13	−0.01	syn	−0.20
Tb II	3899.19	0.37	0.33	syn	−0.47
Dy II	3996.69	0.59	−0.26	syn	0.43
Dy II	4050.57	0.59	−0.47	syn	0.45
Dy II	4073.12	0.54	−0.32	syn	0.43
Dy II	4077.97	0.10	−0.04	syn	0.45
Dy II	4103.31	0.10	−0.38	syn	0.48
Ho II	3398.94	0.00	0.41	syn	−0.19
Ho II	3416.44	0.08	0.26	syn	−0.46
Ho II	3453.11	0.08	0.01	syn	−0.24
Ho II	3456.01	0.00	0.76	syn	−0.21
Ho II	3474.27	0.08	0.28	syn	−0.23
Ho II	3484.83	0.08	0.28	syn	−0.35
Ho II	3810.71	0.00	0.19	syn	−0.33
Ho II	3890.97	0.08	0.46	syn	−0.41
Ho II	4045.45	0.00	−0.05	syn	−0.27
Er II	3499.11	0.06	0.29	57.1	0.14
Er II	3559.89	0.00	−0.69	17.4	0.26
Er II	3616.57	0.00	−0.31	26.3	0.10
Er II	3633.54	0.00	−0.53	28.3	0.36
Er II	3896.23	0.06	−0.12	49.6	0.18
Tm II	3462.20	0.00	0.03	syn	−0.71
Tm II	3761.91	0.00	−0.43	syn	−0.83
Tm II	3795.17	0.03	−1.58	syn	−0.45
Tm II	3848.02	0.00	−0.14	syn	−0.65
Tm II	3996.51	0.00	−1.20	syn	−0.48
Yb II	3694.19	0.00	−0.30	syn	0.02
Hf II	4093.15	0.45	−1.15	syn	−0.03
Os I	4420.46	0.00	−1.43	syn	0.90
Ir I	3513.65	0.00	−1.26	syn	<1.53
Th II	4019.12	0.00	−0.23	syn	−0.60
U II	3859.57	0.04	−0.07	syn	< −0.59

NOTE— "syn" denotes spectrum synthesis was used to measure the abundance.